Applied Thermal Engineering 228 (2023) 120526

Contents lists available at ScienceDirect

Applied Thermal Engineering

journal homepage: www.elsevier.com/locate/apthermeng

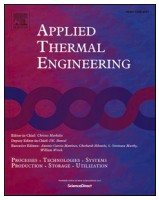

Research Paper

# Design and optimization study of discrete inclined ribs enhanced bend tube based on "Diamond" active cooling thermal protection systems of hypersonic aircraft

Yancong Qiao [a], Wei Liu [b], Zhichun Liu [a,b,*]

[a] China–EU Institute for Clean and Renewable Energy, Huazhong University of Science and Technology, Wuhan 430074, China
[b] School of Energy and Power Engineering, Huazhong University of Science and Technology, Wuhan 430074, China

ARTICLE INFO

*Keywords:*
Discrete inclined ribs
Active thermal protection
Double–symmetrical longitudinal swirl
Secondary circulation
Artificial neural network

ABSTRACT

When the hypersonic aircraft cruises, the surface will generate huge aerodynamic heating. Aiming at the thermal protection of hypersonic aircraft, this paper presented a study on the thermal–hydraulic and thermodynamic performance of discrete inclined ribs enhanced bend tube based on the designed "Diamond" channel. Meanwhile, a comprehensive numerical investigation was carried out for different models. The fluid velocity was found to vary in the range of 0.1–3.5 $m{\cdot}s^{-1}$, with the corresponding Reynolds number ranging from 3600 to 127000. The inlet temperature of heat transfer fluid was set to 253 K. It was visible that double–symmetrical longitudinal swirl was generated under a single upper and lower arrangement (Model D), which led to the best cooling performance on the inner wall. The performance evaluation criteria (*PEC*) and efficiency evaluation criterion (*EEC*) reached 0.99–1.18 and 0.66–1.00, respectively. The effect of four geometrical parameters (height–width ratio($H/d$), length–width ratio ($L/d$), group number of ribs ($n$), and tilt angle ($\alpha$)) of which the ranges are 0.5–2.5, 1.0–4.0,6–15 and 0°–90°, separately, was explored. The results showed that the inner wall temperature decreased up to 4.4 K when the Reynolds number was 72000. The Nusselt number and friction factor increased about 9.9 %–28.8 % and 16.5 %–111.5 %. Efficiency evaluation criterion reached 0.43–0.96. It was found that the combination of parameters would significantly affect the distribution of longitudinal swirls under the influence of secondary circulation in the bend tube. Moreover, many pairs of small vortices near the wall could improve active thermal protection performance. After obtaining the fitting function through the artificial neural network (ANN), the genetic algorithm (GA) was applied to obtain the Pareto front. The design variable for the $L/d = 3.19$, $n = 11$, and $\alpha = 14.3°$ was selected as the optimal solution by the TOPSIS method. When Reynolds number is 72000, the corresponding $T_{in}$ and $\Delta P$ were 261.86 K and 2471.2 Pa. The performance evaluation criteria and efficiency evaluation criterion reached 1.02 and 1.09, respectively. Furthermore, a design variable for the $L/d = 3.0$, $n = 11$, and $\alpha = 15°$ was given for ease of engineering. The present work verified the feasibility of realizing heat transfer enhancement by combining the secondary circulation with longitudinal swirls formed by bend tube and discrete inclined ribs and proposed a new design scheme of active cooling thermal protection systems (ACTPS).

## 1. Introduction

Hypersonic aircraft is gradually becoming the strategic development direction of civil and military aerospace engineering in the 21st century. With the increase of cruise time and Mach number in hypersonic flight, the surface and electronic devices are confronted with severe thermal environment challenges. Extensive experiment results show that air temperature and wall temperature near the hypersonic aircraft's leading edge, wing and tail of hypersonic aircraft are the highest [1,2]. Therefore, the thermal protection system is a vital component of hypersonic aircraft [3]. Thermal protection systems can usually be divided into passive, semi-passive, and active types depending on the heat flux density and heating duration [4].

Passive cooling thermal protection system (PCTPS) mainly relies on the material itself to absorb heat or radiate outward. Its structural design does not affect the aerodynamic configuration of hypersonic aircraft. The C/C thin shell structure, ceramic rigid insulation tile and flexible

* Corresponding author.
*E-mail address:* zcliu@hust.edu.cn (Z. Liu).

https://doi.org/10.1016/j.applthermaleng.2023.120526
Received 7 December 2022; Received in revised form 26 February 2023; Accepted 30 March 2023
Available online 6 April 2023

**Nomenclature**

| | |
|---|---|
| ACTPS | active cooling thermal protection system |
| AFRL | Air Force Research Laboratory |
| ANN | artificial neural network |
| ANOR | analysis of range |
| $C$ | perimeter (mm) |
| CFD | computational fluid dynamic |
| $Cp$ | specific heat capacity ($J{\cdot}kg^{-1}{\cdot}K^{-1}$) |
| $Cr$ | correction coefficient of secondary circulation |
| $D$ | the characteristic length of channel section (mm) |
| DACTPS | "Diamond" active cooling thermal protection system |
| $d$ | rib width (mm) |
| $EEC$ | efficiency evaluation coefficient |
| $f$ | friction factor |
| FVM | finite volume method |
| GA | genetic algorithm |
| $H$ | rib height (mm) |
| $H/d$ | height–width ratio of rib |
| $h$ | convective heat transfer coefficient ($W{\cdot}m^{-2}{\cdot}K^{-1}$) |
| $K_f$ | thermal conductivity of fluid ($W{\cdot}m^{-1}{\cdot}K^{-1}$) |
| $K_S$ | thermal conductivity of solid ($W{\cdot}m^{-1}{\cdot}K^{-1}$) |
| $L$ | rib length (mm) |
| $L/d$ | length–width ratio of rib |
| $l$ | total length of channel (mm) |
| $M$ | correction coefficient of abnormal section |
| MSE | mean square error |
| NSGA-II | non-dominated sorting genetic algorithm |
| $Nu$ | Nusselt number |
| $n$ | group number of ribs |
| $\Delta P$ | pressure drop (Pa) |
| PCTPS | Passive cooling thermal protection system |
| $PEC$ | performance evaluation coefficient |
| $Pr$ | Prandtl number |
| $R$ | range |
| RANS | Reynolds averaged Navier–Stokes |
| $Re$ | Reynolds number |
| Reg | Regression coefficient |
| $S$ | area ($mm^2$) |
| SPCTPS | Semi–passive cooling thermal protection system |
| T | temperature (K) |
| TKE | turbulent kinetic energy |
| TOPSIS | technique for order preference by similarity to ideal solution |
| $u$ | fluid velocity ($m{\cdot}s^{-1}$) |

*Greek symbols*

| | |
|---|---|
| $\rho$ | density of fluid ($kg{\cdot}m^{-3}$) |
| $\lambda$ | thermal conductivity ($W{\cdot}m^{-1}{\cdot}K^{-1}$) |
| $\mu$ | dynamic viscosity of fluid ($kg{\cdot}m^{-1}{\cdot}s^{-1}$) |
| $\Phi$ | diameter of the leading (mm) |
| $\theta$ | distributing angle of ribs (°) |
| $\alpha$ | tilt angle of rib (°) |

*Subscripts*

| | |
|---|---|
| i | j tensor |
| 0 | smooth tube |
| w | wall |
| m | mean |
| f | fluid |
| s | solid |
| in | inner wall |
| T | temperature |
| P | pressure |

insulation blanket were used for PCTPS during the atmospheric reentry of the American Shuttle and the space shuttle Buran of the USSR [5]. Around 2000, NASA [6,7] developed a new reusable thermal insulation material CRI which was successfully applied in flight tests. Recently, the frequency of rocket launches around the world has gradually increased. The birth of reusable rockets will greatly promote the development of the human space industry. Nevertheless, the disadvantages of PCTPS, which are expensive and cannot be reused are gradually exposed.

Semi–passive cooling thermal protection system (SPCTPS) combines heat pipe with ablation structure to absorb heat. Liu et al. [8] studied the SPCTPS of C/C composite with built–in heat pipes and proved it is an efficient thermal protection method. In 2009, Air Force Research Laboratory (AFRL) [9] completed the validation test of high-temperature heat pipe cooling in the leading edge, proving that SPCTPS can significantly reduce the consumption of ablation materials. However, whether the high–temperature heat pipe and ablation structure are precisely matched will remarkably affect the performance of the thermal protection structure. Subsequently, it is still a problem to solve how the arrangement of heat pipes meets the aerodynamic configuration of hypersonic aircraft.

In contrast, an active cooling thermal protection system (ACTPS) with hydrocarbon fuel as coolant is one of the most effective methods for thermal protection of hypersonic aircraft [10]. Liu et al. [11] investigated a sweating active cooling thermal protection structure, which can increase the heat capacity by at least 70 %. Hou et al. [12] reviewed the cooling performance of a double honeycomb sandwich convective cooling structure. The results showed that the structure effectively blocks heat transfer to the inner layer. Chen et al. [13] proposed an active film cooling method, which can form a low–temperature film, reducing the ablation of the leading edge. Meanwhile, scramjet engines based on regenerative cooling technology and heat transfer enhancement mechanism have been gradually applied in recent years [14,15]. Zhu et al. [16] examined and verified the feasibility of three active cooling methods, i.e., regenerative cooling, film cooling, and transpiration cooling, and profoundly analyzed the mechanism of each cooling method.

ACTPS is the critical technology to solve the thermal load problem of hypersonic aircraft, space transportation systems and advanced aero engines [4]. It has been verified that endothermic hydrocarbon fuel has good thermal–hydraulic and thermodynamic performance while being used in ACTPS [10,17,18]. Hypersonic aircraft investigation is a great systematic project developing towards integrating "function, low cost and high structural efficiency" [3]. For the benefit of extended–term reusability, the cooling process requires a valid active rather than passive protection method [19].

ACTPS rejects heat through a convective heat transfer process between the coolant and solid materials, realizing the protection of the internal electronic devices. Thus, heat transfer enhancement has gradually become an efficacious method to improve the cooling efficiency of ACTPS. Recently, scholars have obtained the optimal flow field pattern in the tube, which provides a new idea for designing new efficient heat transfer enhancement technology [20]. To minimize potential energy dissipation during heat convection, Guo et al. [21–25] determined that the longitudinal swirl is the main characteristic of the optimal velocity field and proposed a concept of heat transfer optimization based on the field synergy principle. Liu et al. [26–30] extended the field synergy principle and indicated that longitudinal swirl effectively balances the contradiction between heat transfer enhancement and power consumption increase.

Sriromreun et al. [31] calculated the effect of baffle turbulence on

heat transfer enhancement in rectangular channels and found that the Z–shaped baffle significantly impacts the thermal–hydraulic and thermodynamic performance. Wang et al. [32] proposed a longitudinal swirl generator of symmetric wings (SWLSGs) and analyzed the results from the field synergy perspective and the entropy generation. SWLSGs play a good role in disturbing the fluid, strengthening the convective heat transfer effect. Zheng et al. [33,34] reported that the discrete inclined rib–groove could improve the heat transfer performance without significantly increasing pressure drop. Cheng et al. [35] investigated the heat transfer and flow characteristics of twisted tubes of different cross-section shapes, which can greatly improve thermal–hydraulic and thermodynamic performance. Tang et al. [36] conducted the numerical simulation to verify the mechanism of multi–vortices longitudinal swirled heat transfer enhancement and investigated the influence of the arrangement of discontinuous crossed ribs and grooves along the flow direction. Gunnasegaran P et al. [37] designed a new microchannel combined with a longitudinal swirl generator. It was found that better uniformities in heat transfer coefficient and temperature could be obtained in heat sinks having the most minor hydraulic diameter. Li et al. [38] performed an experiment on circular tubes with rectangular winglets, trapezoidal winglets, and triangular winglets. The results showed that the comprehensive performance is the best, and the *PEC* value is 0.97–1.07 when four pairs of trapezoidal winglets are arranged in each row. A large amount of numerical and experimental results showed that the larger the longitudinal swirl intensity based on the field synergy principle, the more apparent the enhancement performance.

Qiao et al. [39] investigated the thermal–hydraulic and thermodynamic performance of circular, rectangular and pentagonal bend tubes in ACTPS of hypersonic aircraft, and according to whether the cooling effect and structural strength meet the requirements, a diamond-shaped channel was proposed, which was called “Diamond” active cooling thermal protection system (DACTPS). The elbow shape of DACTPS could form secondary circulation, improving the active cooling performance inside the bend tube.

In the present study, the discrete inclined ribs are applied and improved based on the DACTPS to obtain a better cooling effect on hypersonic aircraft. The numerical results showed that the cooling effect of DACTPS could be significantly enhanced by adding discrete inclined ribs to the smooth tube. Different arrangements are compared at a larger Reynolds number range, and the four parameters’ thermal–hydraulic performance is analyzed. It is found that the discrete inclined ribs enhanced bend tube realizes a coupling mechanism of flow and heat transfer enhancement. The secondary circulation generated by the leading edge curvature of DACTPS and longitudinal swirls generated by the discrete inclined ribs cooperates to achieve heat transfer enhancement with higher overall thermal–hydraulic performance, thereby improving the active cooling performance for hypersonic aircraft.

Recently, there have been many types of research on heat transfer enhancement of the circular, straight tube, but few studies on flow and heat transfer characteristics of the irregular–shaped bend tube. This paper designs and presents a study on the discrete inclined ribs enhanced bend tube based on the DACTPS. The feasibility of realizing heat transfer enhancement by combining the secondary circulation with longitudinal swirls formed by rib turbulence is verified. This method has superior thermal hydraulic performance at a larger Reynolds number range, which meets the active thermal protection requirements with lower pressure drop. Our paper aims to propose a new design scheme for ACTPS and provide some experience and guidance for the design of ACTPS for hypersonic aircraft.

## 2. Description of discrete discontinuous inclined ribs enhanced bend tube

The overall model based on the designed DACTPS [39] is present in Fig. 1 (a). A channel unit is selected for analysis simulation to save computational resources, as shown in Fig. 1 (b). The diamond-shaped section is also demonstrated in Fig. 1 (b) particularly. Locally enlarged graph and parameter representation of the channel unit is provided in Fig. 2. It is visible that discrete inclined ribs have application in the leading edge region to meet the heat protection requirements, while no inclined ribs on leeward and windward region, for reasons of minimizing structural weight. The parameters of the inclined rib are listed in Table 1. Since the DACTPS is the bending channel, discrete inclined ribs are defined to be distributed at 0–81° ($\theta$) of the leading edge. The ribs on the same plane are a group. $n$ represents the number of rib groups. Rib width ($d$) is set to 1.0 mm. Then, definitions of Height–weight ratio ($H/d$) and Length–weight ratio ($L/d$) are given for subsequent studies.

Fig. 3 presents several arrangements of discrete inclined ribs. To better compare the different arrangements, five fluid–solid coupling surfaces are numbered on the leading edge, and each serial number has the same color as the surface, as depicted in Fig. 3 (b) and (c). In accordance with the view direction to spread five surfaces, Model A has two groups of ribs on the upper and lower surfaces, respectively. Furthermore, the other four arrangements and size parameters are shown in Fig. 3 (c).

## 3. Research methods

### 3.1. Assumption

To simplify the numerical simulation, the fluid is assumed as a continuous incompressible fluid.

The effects of gravity and radiation are ignored, and the physical properties such as density ($\rho$), thermal conductivity ($\lambda$), dynamic viscosity ($\mu$), and specific heat capacity ($Cp$) are constant. The flow field is governed by the three–dimensional Reynolds averaged Navier–Stokes (RANS) equations, based on the assumption that the heat transfers and flow processes are turbulent and steady, and the heat loss to the

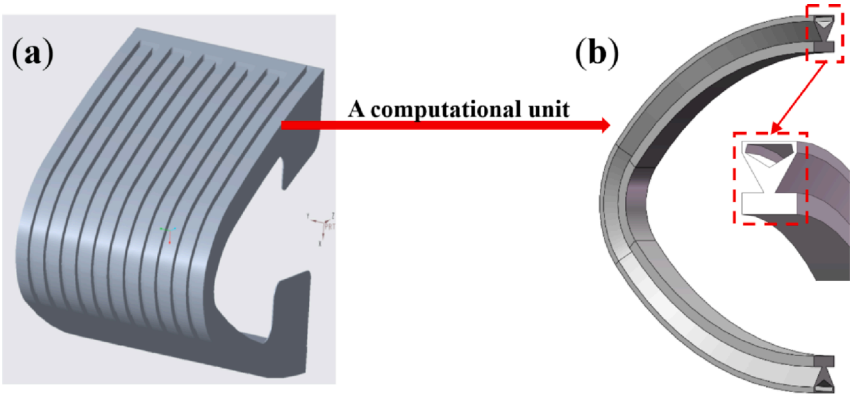


**Fig. 1.** Overall model and channel unit.

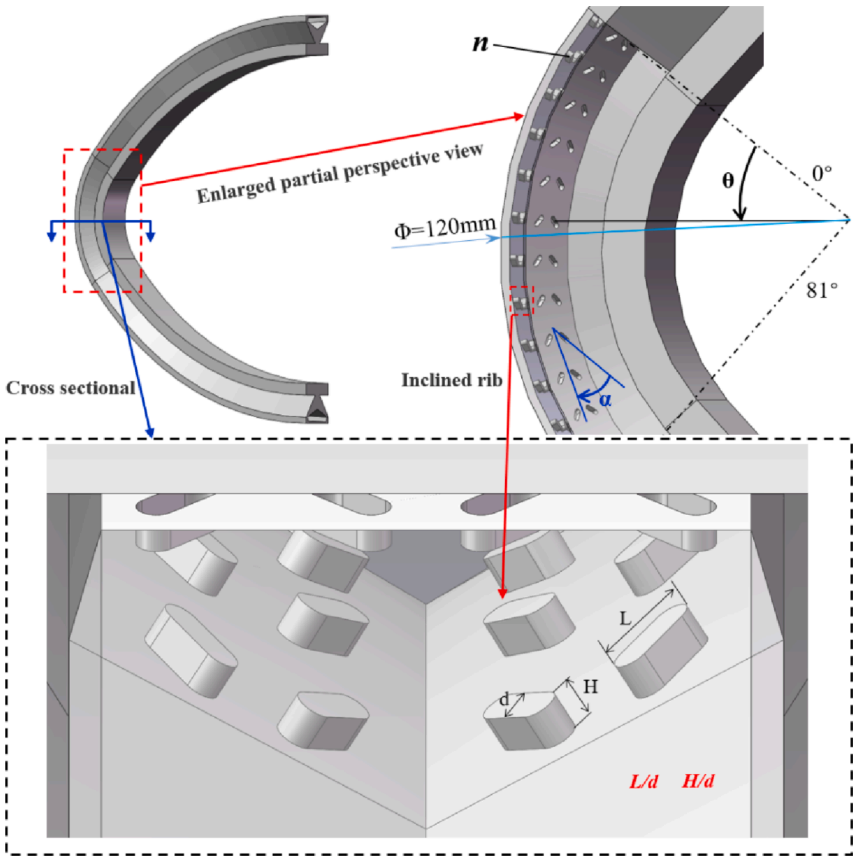


**Fig. 2.** Locally enlarged graph and parameter representation.

**Table 1**
Parameter of discrete inclined ribs.

| Parameter | value |
|---|---|
| Diameter of leading, $\Phi$(mm) | 120 |
| Distributing angle, $\theta$(°) | 0–81 |
| Group number of ribs, $n$ | 12 |
| Tilt angle, $\alpha$(°) | 45 |
| Rib width, $d$(mm) | 1.0 |
| Rib height, $H$(mm) | 1.0 |
| Rib length, $L$(mm) | 2.5 |
| Height–width ratio, $H/d$ | 1.0 |
| Length–width ratio, $L/d$ | 2.5 |

environment is neglected [34].

### 3.2. Governing equations

The governing equations are implemented using the ANSYS Fluent based on the finite volume method (FVM). The convergence criterion in this study states that the relative residual values are less than $10^{-3}$ for the continuity equation and less than $10^{-6}$ for all other variables. All the relative residual values are maintained constant [40]. The pressure outlet is adopted to reduce backflow, and a second-order upwind scheme is employed to discretize the governing equations for momentum and energy. The SIMPLE algorithm is applied to achieve the coupling between velocity and pressure. The governing equations are given as follows:

Continuity equation:

$$\frac{\partial(\rho u_i)}{\partial_{X_i}} = 0 \tag{1}$$

Momentum equation:

$$\frac{\partial}{\partial_{X_j}}(\rho u_i u_j) = -\frac{\partial \rho}{\partial_{X_j}} + \frac{\partial}{\partial_{X_j}}\left[\mu\left(\frac{\partial_{u_i}}{\partial_{X_j}} + \frac{\partial_{u_j}}{\partial_{X_i}}\right)\right] - \frac{2}{3}\mu\frac{\partial_{u_i}}{\partial_{X_j}}\delta_{ij} + \frac{\partial}{\partial_{X_j}}\left(\rho\overline{u_i' u_j'}\right) \tag{2}$$

Energy equation:

$$\frac{\partial}{\partial_{X_i}}(\rho u_i c_p T) = \frac{\partial}{\partial_{X_i}}\left(k\frac{\partial T}{\partial_{X_i}}\right) \tag{3}$$

Heat conduction equation in solid domain:

$$\frac{\partial}{\partial_{X_i}}\left(K_s\frac{\partial T}{\partial_{X_i}}\right) = 0 \tag{4}$$

where $Ks$ is the thermal conductivity of solid material, $\mu$ is the dynamic viscosity coefficient, and $Cp$ is specific heat capacity.

Among the several turbulent models utilizable for closure of the governing equations, the shear stress tensor $k$–$\omega$ Model (SST $k$–$\omega$) proposed by Wilcox [41] and Menter [42] has demonstrated good behavior in modeling adverse pressure gradients and separation flow because of the combination of the $k$–$\omega$ Model near walls and the $k$–$\varepsilon$ Model in the free stream. Transport equations are as follows [43]:

$$\frac{\partial}{\partial_{X_i}}(\rho k u_i) = \frac{\partial}{\partial_{X_i}}\left(\Gamma k\frac{\partial k}{\partial_{X_i}}\right) + G_k + Y_k \tag{5}$$

$$\frac{\partial}{\partial_{X_i}}(\rho\omega u_i) = \frac{\partial}{\partial_{X_i}}\left(\Gamma\omega\frac{\partial\omega}{\partial_{X_i}}\right) + G_\omega + Y_\omega \tag{6}$$

### 3.3. Boundary conditions

Three heat fluxes of 110 W, 660 W, and 1375 W are applied to the leeward, windward, and leading-edge surfaces to simulate the aerodynamic heating of hypersonic aircraft, as displayed in Fig. 4. Meanwhile, all other outer surfaces are set to heat insulation. The cooling

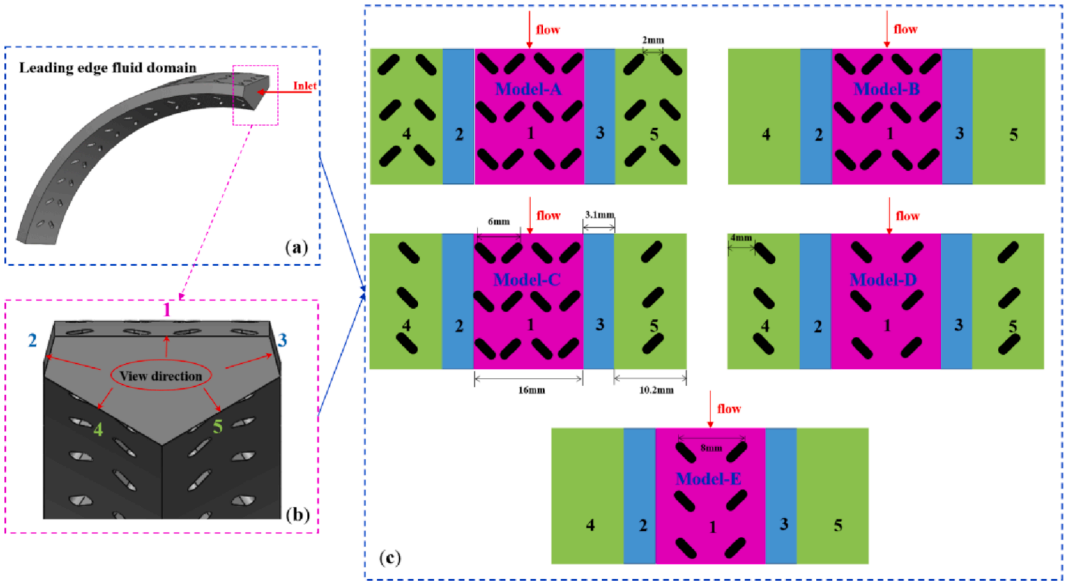


**Fig. 3.** Discrete inclined ribs arrangement.

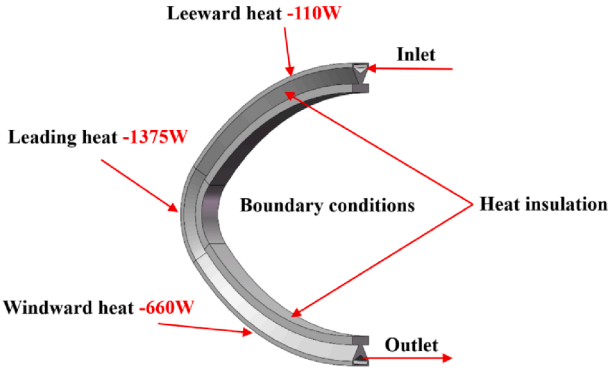


**Fig. 4.** Boundary conditions of channel unit.

medium is aviation kerosene RP–3, of which inlet velocity increases from 0.1 m·s$^{-1}$ to 3.5 m·s$^{-1}$, and the corresponding Reynolds number is in the range of 3600–127000. Qiao et al. [39] studied the influence of three inlet temperatures of a heat transfer fluid on the thermal–hydraulic and thermodynamic performance of the ACTPS. It was proved that the inlet temperature has no effect on the flow state in the channel, and the impact on the inner wall temperature is linear. Therefore, the inlet temperature of heat transfer fluid is set to 253 K in the present study.

### 3.4. Thermal properties

Because compared to liquid water, the dynamic viscosity ($\mu$) of RP–3 is only a fifth of that of water. RP–3 is seen as the incompressible Newtonian fluid of which thermal properties are constant, as listed in Table 2. The reference temperature and pressure for the thermal properties in Table 2 are 293 K and standard atmospheric pressure, respectively. Nickel–based alloy Inconel–625 is applied as the solid material in the present study for its better temperature tolerance ability and low density [44], and its thermal properties, of which the reference temperature is 500 K, are listed in Table 3. $Cp$ is the specific heat capacity of materials. $K_f$ and $K_S$ are the thermal conductivity of the fluid and solid material, respectively.

**Table 2**
Thermal properties comparison of fluid.

| Fluid | $\rho$ (kg·m$^{-3}$) | $Cp$ (J·kg$^{-1}$·K$^{-1}$) | $K_f$ (W·m$^{-1}$·K$^{-1}$) | $\mu$(kg·m$^{-1}$·s$^{-1}$) |
|---|---|---|---|---|
| RP–3 | 800 | 2100 | 0.13 | 0.0001984 |
| Water | 998.2 | 4182 | 0.60 | 0.001003 |

### 3.5. Parameter definitions

In the present simulation, The Reynolds number ($Re$) is defined as follows [45,46]

$$Re = \frac{\rho u_m D_h}{\mu} \tag{7}$$

$$D_h = \frac{4S}{C} \tag{8}$$

where $S$, $C$ and $D_h$ are the area, perimeter and characteristic length of the channel section, respectively; $u_m$ is the average velocity of inlet, and $\mu$ is the dynamic viscosity of fluid.

Friction factor ($f$) and total pump power ($Wp$) can be calculated by following expression

$$f = \frac{2\Delta P D_h}{\rho l (u_m)^2} \tag{9}$$

$$W_P = \frac{m\Delta P}{\rho} \tag{10}$$

here, $\Delta P$ is the pressure drop between the inlet and outlet; $l$ is the total length of DACTPS channel, which are valued 520 mm; $m$ is the mass flow rate of fluid.

The convective heat transfer coefficient $h$ can be expressed as

$$h = \frac{q}{(T_w - T_m)} \tag{11}$$

where $Tw$ and $Tm$ are the average temperature of solid and fluid surface

**Table 3**
Thermal properties of Inconel-625.

| Properties | $\rho$ (kg·m$^{-3}$) | $Cp$ (J·kg$^{-1}$·K$^{-1}$) | $K_S$ (W·m$^{-1}$·K$^{-1}$) | $\mu$(kg·m$^{-1}$·s$^{-1}$) |
|---|---|---|---|---|
| Value | 8440 | 480 | 14 | \ |

on fluid–solid coupling domain. Subsequently, Nusselt number (*Nu*) can be calculated by Eq. (12), as follows [47]

$$Nu = \frac{hD_h}{K_f} \tag{12}$$

where $K_f$ is the thermal conductivity of RP–3 and its value is 0.13 $W{\cdot}m^{-1}{\cdot}K^{-1}$.

To evaluate the thermal–hydraulic and thermodynamic performance of discrete inclined ribs enhanced bend tube at an identical *Re*, the extensively used performance evaluation criteria (*PEC*) and efficiency evaluation criterion (*EEC*) are applied in the present study. The *EEC* and *PEC* [48] are calculated from the following formula:

$$EEC = \frac{Nu/Nu_0}{f/f_0} \tag{13}$$

$$PEC = \frac{Nu/Nu_0}{(f/f_0)^{1/3}} \tag{14}$$

where $Nu_0$ and $f_0$ are the Nusselt number and the friction factor in the smooth tube, respectively.

## 4. Grid independence test and model validation

### 4.1. Grid system and independence test

The 3D geometrical models and grid systems are executed by commercial programs SolidWorks and ICEM–CFD, respectively. As shown in Fig. 5, hexahedral grids are adopted as the main mesh structure for the solid domains, while tetrahedral grids are generated for the fluid and rib domain. Fig. 5 (c) presents that 14 boundary layer refinements are applied to fluid–solid coupling surface and the first layer grid size is 0.02 mm. Simultaneously, grids of the leading edge region are encrypted, and the grid size of windward and leeward regions is appropriately increased due to a simple flow state.

Five different grid systems, with $5 \times 10^5$, $1 \times 10^6$, $2 \times 10^6$, $4 \times 10^6$ and $1.15 \times 10^7$ mesh elements, are generated for model A to perform a grid independence test at a *Re* of 72635. It is visible from Fig. 6 that the relative errors of *Nu* and *f* between the grid systems with $5 \times 10^5$ and $1.15 \times 10^7$ are 2.7 % and 17.6 %, while the relative errors between the grid systems with $4 \times 10^6$ and $1.15 \times 10^7$ are 0.8 % and 2.8 %, respectively. Hence, the grid system with $4 \times 10^6$ elements is considered sufficiently dense for the numerical analysis. Accordingly, the grid system with $4 \times 10^6$ elements is adopted to perform the subsequent simulations.

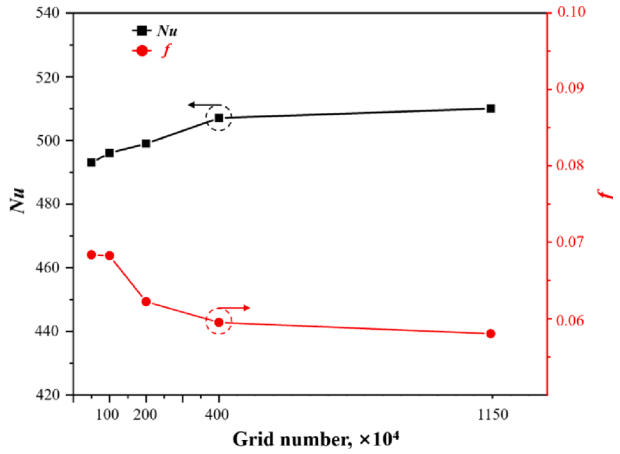


**Fig. 6.** Grid independence test.

### 4.2. Model verification

Petukhov's and Gnielinski's correlation [49,50] for the *Nu* and the *f*, respectively, are given in Eqs. (15) and (16). Meanwhile, related correction coefficients are given in Eqs. (17) – (19), as follows:

$$f_0 = (1.82lgRe - 1.64)^{-2} \tag{15}$$

$$Nu_0 = \frac{(f/8)(Re - 1000)Pr.M.Cr}{1 + 12.7(f/8)^{0.5}(Pr^{2/3} - 1)} \tag{16}$$

$$Pr = \frac{\mu C_p}{K_f} \tag{17}$$

$$M = \left[1 + (D_h/L)^{2/3}\right] \tag{18}$$

$$Cr = 1 + 10.3(2D_h/\Phi)^3 \tag{19}$$

where *Pr* is the Prandtl number [51] which can reflect the interaction between energy and momentum transfer process, playing an important role in the thermodynamic calculation. The *Pr* of RP–3 is 3.2049, calculated from thermal properties in Table 2. *M* and *Cr* are the correction coefficient of irregular section and secondary circulation in the spiral tube, respectively. Since DACTPS is a curve–shaped channel to fit the aerodynamic layout of hypersonic aircraft, the effect of heat transfer enhancement caused by the secondary circulation cannot be

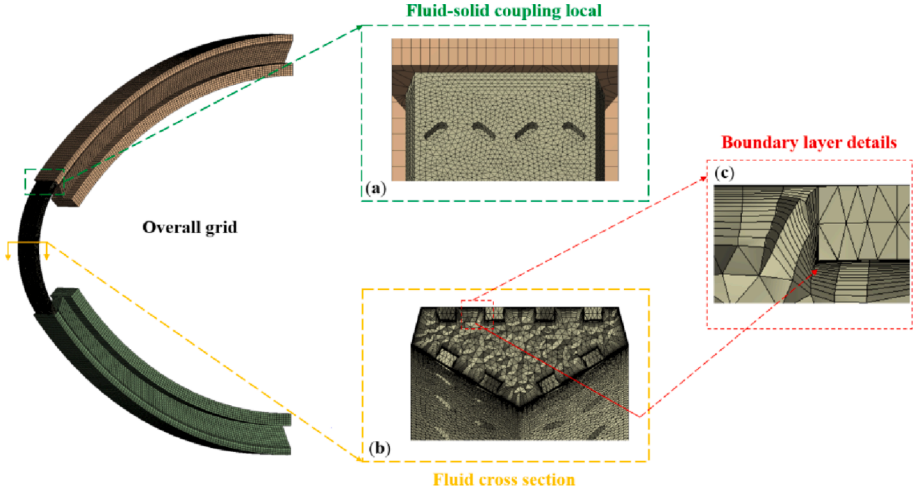


**Fig. 5.** Grid system for channel unit.

ignored.

A comparison between numerical results and correction is depicted in Fig. 7. It is found that the average deviations of the *Nu* and *f* are about 8 % and 14 %, respectively. Therefore, the numerical process adopted in the present investigation for heat transfer and flow resistance predictions is judged to be dependable.

## 5. Results and discussion

### 5.1. Heat transfer enhancement mechanism

#### 5.1.1. Flow characteristics and temperature distributions

The flow characteristics and temperature distributions of five enhanced bend tubes are analyzed under the parameter of $\alpha = 45°$, $n = 12$, $H/d = 1.0$ and $L/d = 2.5$. It is visible in Fig. 8 (a) that all five arrangements can significantly reduce the outer wall temperature. Model E has only one pair of inclined ribs with a small heat transfer area, leading to the minimum heat transfer enhancement. However, Model A has four pairs of inclined ribs, which has the best cooling effect on the outer wall. As shown in Fig. 8 (b), the inner wall temperature decreases by more than 150 K in low *Re*. It can be investigated that the cooling effect on the inner wall is related to the number of inclined ribs and depends on the arrangement of discrete inclined ribs. Fig. 8 (c) presents that Model D, with only two pairs of inclined ribs, has the best cooling effect on the inner wall, which is better than Model A, with more inclined ribs. Moreover, the inner wall temperature difference between Model E and Model D is close to 20 K at *Re* of 10895.

Fig. 9 shows the temperature contours of tubes with smooth, Model A and Model D arrangements at *Re* = 18000. It can be seen from Fig. 9 (a) that a large area of the high-temperature region is present on the outer surface of the smooth tube. Still, Model A has a better cooling effect on the outer owing to its double pairs of discrete ribs arrangement, which is consistent with the temperature curve in Fig. 8 (a). Meanwhile, the outer temperature of Model D can be controlled below 610 K.

Fig. 9 (b) presents that the inner wall temperature of the smooth tube reaches 326 K, which cannot meet the normal operation requirement of electronic devices. Model D has the lowest inner wall temperature and temperature gradient. Because of the resistance of four pairs of discrete inclined ribs, the velocity of RP–3 at the leading edge drops sharply, deteriorating the heat transfer enhancement of the subsequent channel at the windward region of Model A, as depicted in Fig. 9 (b).

To explore the reasons for the difference in flow characteristics and temperature distributions of different models, streamline and tangential vectors are investigated, as shown in Fig. 10. Fig. 10 (a) presents the section located at the leading edge. Fig. 10 (b) demonstrates that secondary circulation generated by the smooth tube only improves the heat transfer performance near the wall and hardly mixes the internal fluid

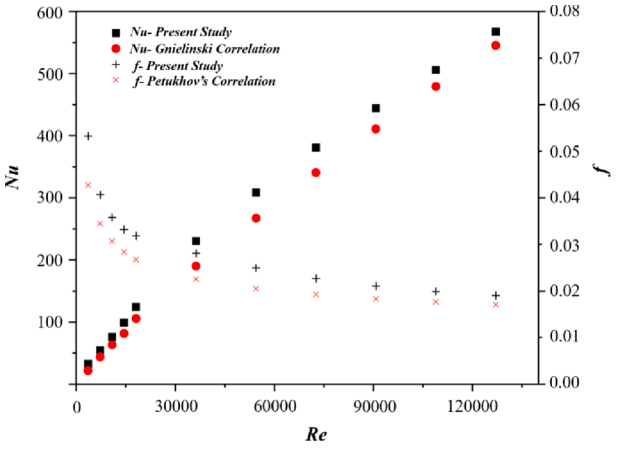


**Fig. 7.** Verification of heat transfer and flow resistance for smooth tube.

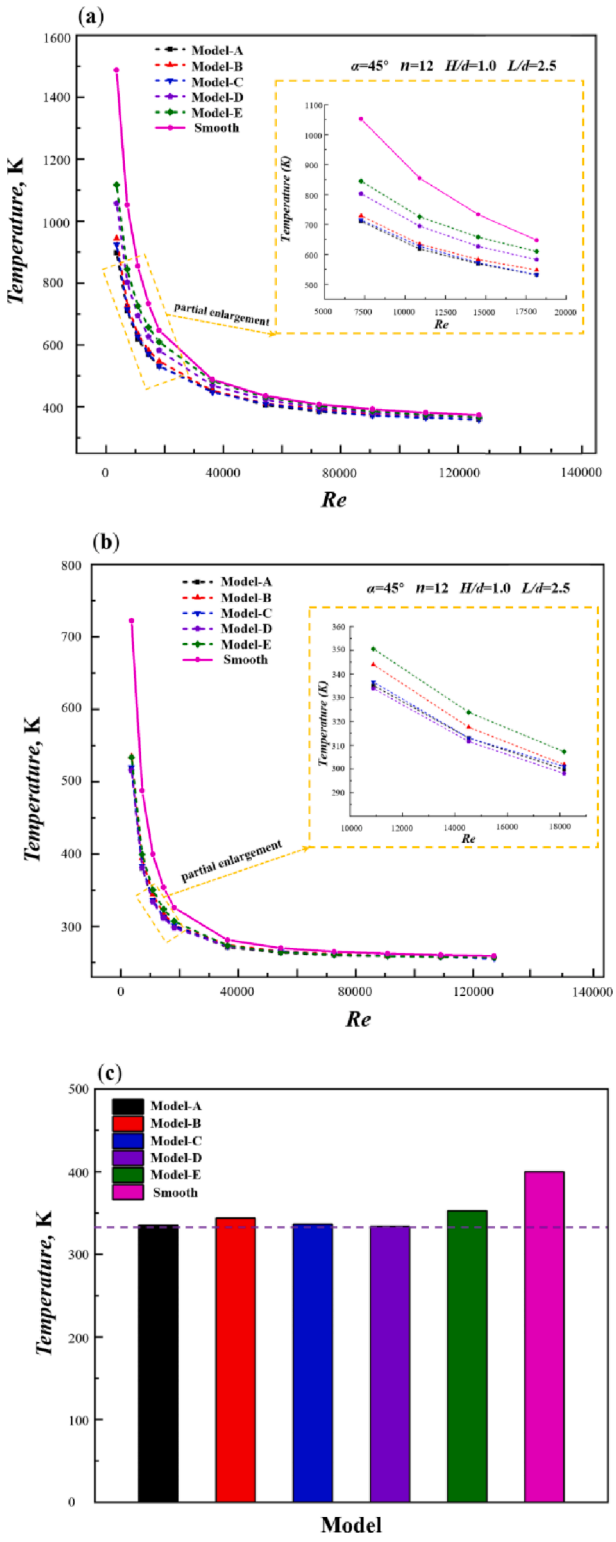


**Fig. 8.** Temperature variation of different models at $\alpha = 45°$, $n = 12$, $H/d = 1.0$, and $L/d = 2.5$: (a) outer wall and (b) inner wall (c) inner wall at *Re* = 10895.

well. Nevertheless, discrete inclined ribs form longitudinal swirls in the leading edge to enhance the heat transfer performance of Model A and Model D. It is visible that double–symmetrical longitudinal swirls are generated under the simultaneous action of secondary circulation, and discrete inclined ribs arrangement of Model D. In Model A, the development of secondary circulation is limited overly by the performance of

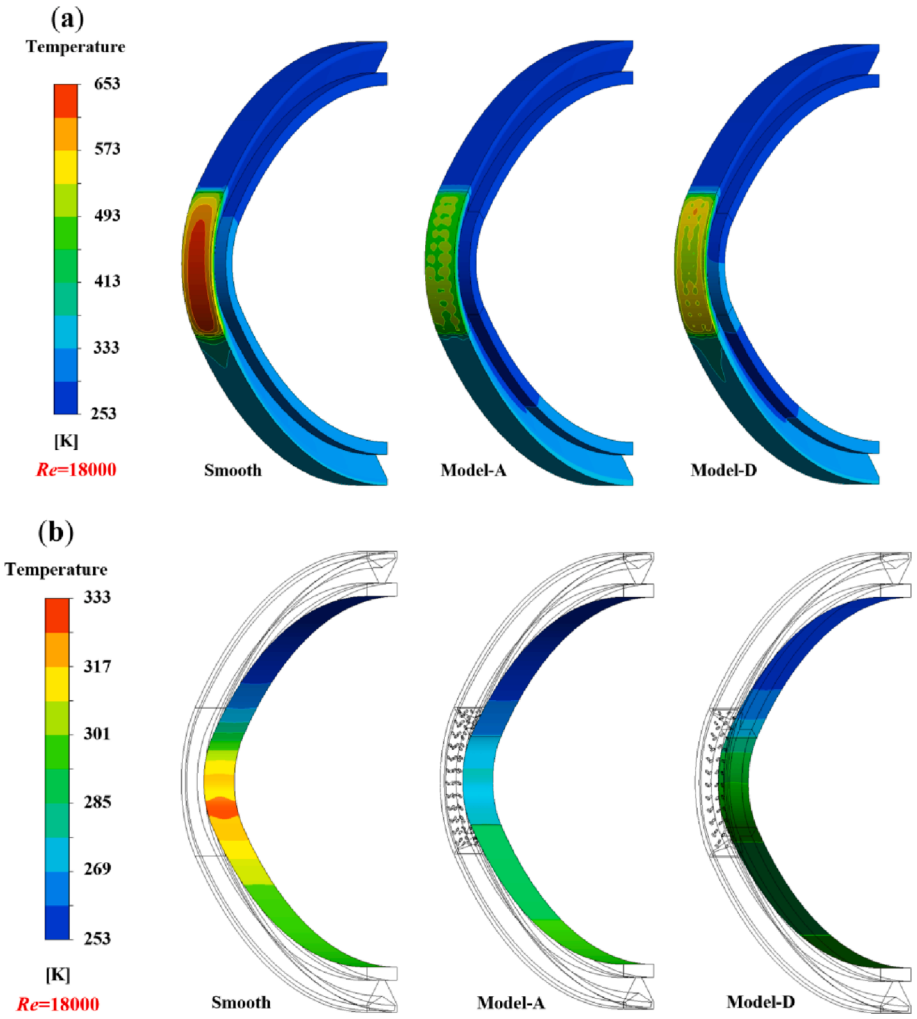


**Fig. 9.** Temperature contours of different models at $\alpha = 45°$, $n = 12$, $H/d = 1.0$, and $L/d = 2.5$: (a) outer wall and (b) inner wall.

four pairs of inclined ribs, causing asymmetrical temperature field and streamline, which is unfavorable to the temperature control of DACTPS.

Fig. 10 (c) shows the tangential vector and solid temperature distribution. A large high-temperature area is present on the outer wall of the smooth tube, circled by red line in the figure. Meanwhile, due to the asymmetrical swirls, the cooling effect on one side is deteriorated of Model A, while Model D forms symmetrical solid temperature distributing uniformly, which is beneficial to the temperature control of DACTPS.

Fig. 11 presents the flow state of Model D at $Re = 18000$, including streamline, as depicted in Fig. 11 (a) and velocity vector, as displayed in Fig. 11 (b). It can be seen from Fig. 11 (a) that the fluid is disturbed by discrete ribs at the leading edge, showing a flow state of spiral forward. In addition, the velocity vector with discrete ribs becomes denser, and fluid disturbance is more intense, which enhances the heat transfer performance near the wall.

It can definitely be concluded from the above research that double–symmetrical longitudinal swirls are formed because of discrete inclined ribs with the arrangement of Model D. Central swirls promote the mixing of internal and near-wall fluid, improving the heat transfer efficiency and swirls on both sides hinder the interference of wall velocity boundary layer, which can strengthen fluid scouring on both sides, reducing the inner wall temperature.

### 5.1.2. Thermal–hydraulic and thermodynamic performance

Fig. 12 shows the convective heat transfer coefficient ($h$) and pressure drop ($\Delta P$) with the $Re$ increasing of different models at $\alpha = 45°$, $n = 12$, $H/d = 1.0$ and $L/d = 2.5$. It is visible from Fig. 12 (a) that the $h$ rises with the increase of $Re$. The smooth tube has the minimum $h$, and the $h$ increases when the number of inclined ribs increases, which is why Model A, with the most ribs has the best cooling effect on the outer wall. The $\Delta P$ increases with the $Re$, as depicted in Fig. 12 (b). At the same $Re$, the $\Delta P$ increases with the number of ribs increasing. It is remarkable that the $\Delta P$ of the smooth tube and Model A reach 5.4 kPa and 15.8 kPa, respectively. Whereas the $\Delta P$ of Model D is 10 kPa, only 63.3 % of Model A significantly reduces the $\Delta P$ caused by inclined ribs.

Fig. 13 shows the variation of $Nu$ and $f$ with the increase of $Re$ under different models. As demonstrated in Eq. (12), $Nu$ should theoretically present the same trend as $h$. It can be investigated in Fig. 13 (a) that discrete inclined ribs significantly improve the $Nu$ of DACTPS, and the $Nu$ increases by 22 %–33 % compared with the smooth tube for five models, showing the same trend as $h$. The $f$ decreases with $Re$, and the smooth tube has the most minor $f$, which is consistent with the study above. It is noteworthy that $f$ is more sensitive to the change of $Re$ in the range of low $Re$, as depicted in Fig. 13 (b).

For the purpose of showing the heat transfer enhancement of discrete inclined ribs visually, Fig. 14 presents thermal–hydraulic performance contour of Model D at $Re = 36000$. It is revealed that high heat flux appears behind each pair of discrete ribs, which is the dark red region depicted in Fig. 14 (a). The unique double–symmetrical longitudinal swirls enhance the heat transfer performance of fluid disturbed by discrete inclined ribs. Fig. 14 (b) and (c) show the turbulent kinetic

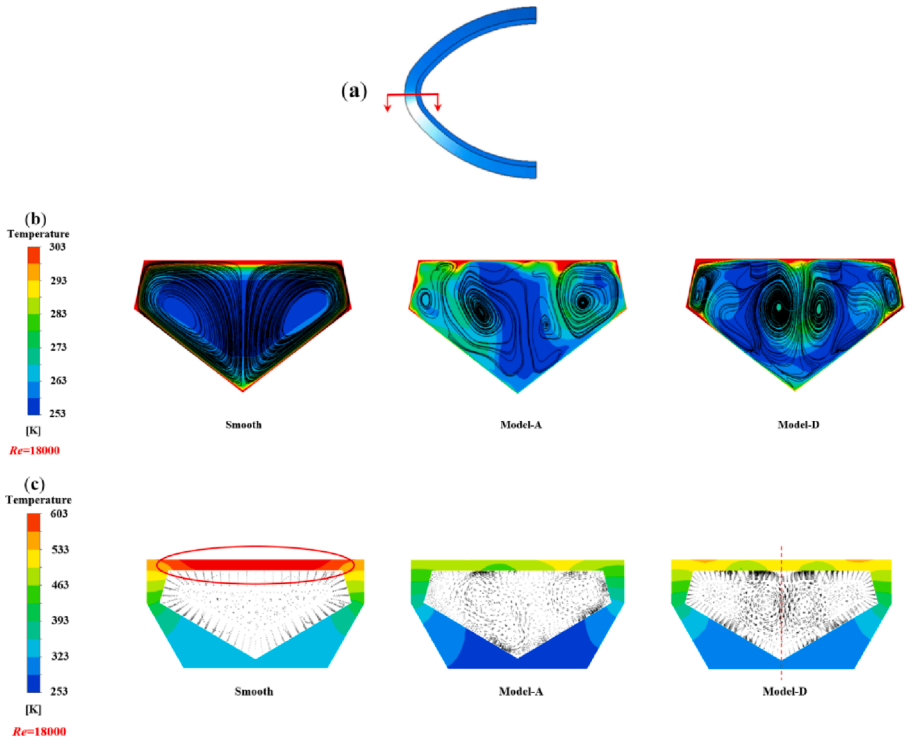


**Fig. 10.** Streamline and tangential vector graph of different models at $Re$ = 18000: (a) section location and (b) streamline and (c) tangential vector.

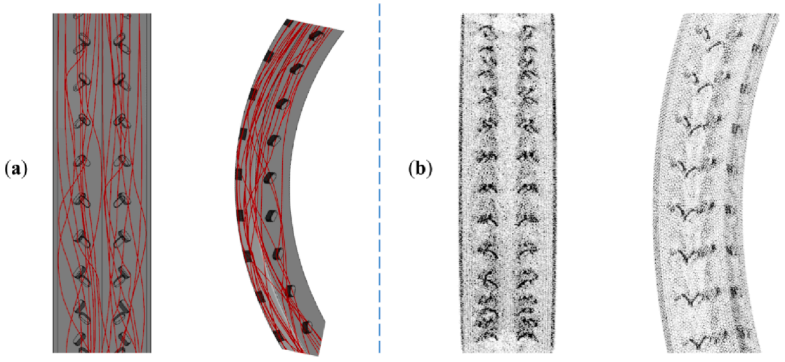


**Fig. 11.** Streamline and velocity vector in leading edge region of Model D at $Re$ = 18000: (a) streamline and (b) velocity vector.

energy (TKE) and eddy viscosity of Model D at $Re$ = 36000, respectively. The corresponding value of the discrete ribs region is obviously higher than that of the smooth tube.

Fig. 15 presents the change of pump power ($Wp$), $PEC$ and $EEC$ with $Re$ of different models at $\alpha = 45°$, $n = 12$, $H/d = 1.0$ and $L/d = 2.5$. It can be seen in Fig. 15 (a) that the variation trend of $Wp$ is consistent with that of the $\Delta P$, which is controlled by Eq. (10). The $Wp$ range of Model D is 0.0002–3.3874 W in the $Re$ range of the present study. Moreover, $Wp$ increases slowly at low $Re$ and rapidly at high $Re$. In Fig. 15 (b), the $PEC$ of Model D is in the range of 0.99–1.18, showing a changing trend of increasing first and decreasing then. It can be investigated from drawings of partial enlargement in Fig. 15 (b) that the comparison regularity of $PEC$ of five models is less evident at the $Re$ transition stage. When $Re$ = 3600, the $PEC$ of Model E is 1.18, which is the lowest $PEC$ of all five models, while when $Re$ goes up to 18000, the $PEC$ of Model E is 1.03, which is the highest $PEC$ of all five models. $EEC$ decreases with $Re$ increases, as illustrated in Fig. 15 (c). It is visible that $EEC$ decreases rapidly at the $Re$ transition stage and decreases slowly at the $Re$ fully turbulent stage. In the range of turbulent $Re$ studied, the $EEC$ of Model D is 0.66–1.00. In addition, it can be found from Fig. 15 (b) and (c) that $EEC$ accurately reflects thermal–hydraulic performance in the turbulence stage, while $PEC$ has no obvious regularity in a range of $Re$.

### 5.2. Effects of parameters on thermal–hydraulic performances

The effects of parameters on thermal–hydraulic performances of Model D are investigated for its best cooling effect on the inner wall and good thermal–hydraulic performances. The primary task of ACTPS of hypersonic aircraft is to reduce the inner wall temperature under high heat flux.

#### 5.2.1. Effects of the rib height–width ratio ($H/d$)

Fig. 16 depicts the temperature of different $H/d$ at $\alpha = 45°$, $n = 12$, and $L/d$ = 2.5. The rib height ($H$) varies from 0.5 mm to 2.5 mm, meaning the height–width ratio ($H/d$) varies from 0.5 to 2.5. The outer wall temperature is close to 1200 K at $Re$ = 3600 and $H/d$ = 0.5, which is lower than the tolerance temperature of Inconel–625, as shown in Fig. 15 (a). It is visible that $H/d$ = 2.5 has the best cooling effect on the outer wall for its largest heat transfer area. While the cooling effect is not only affected by the heat transfer area. It can be investigated from

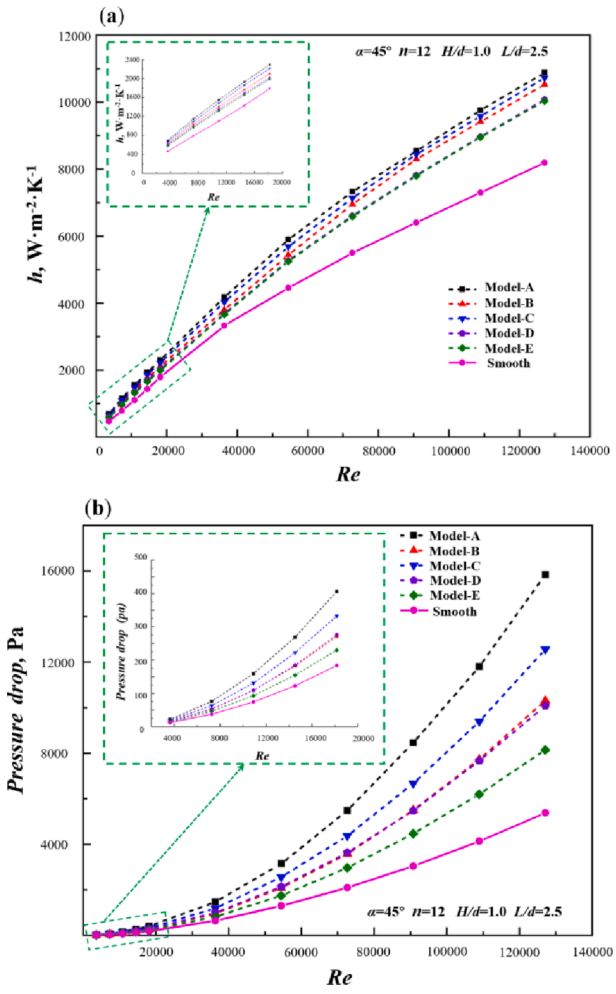


**Fig. 12.** Convective heat transfer coefficient ($h$) and pressure drop ($\Delta P$) diagrams at $\alpha = 45°$, $n = 12$, $H/d = 1.0$, and $L/d = 2.5$: (a) $h$ and (b) $\Delta P$.

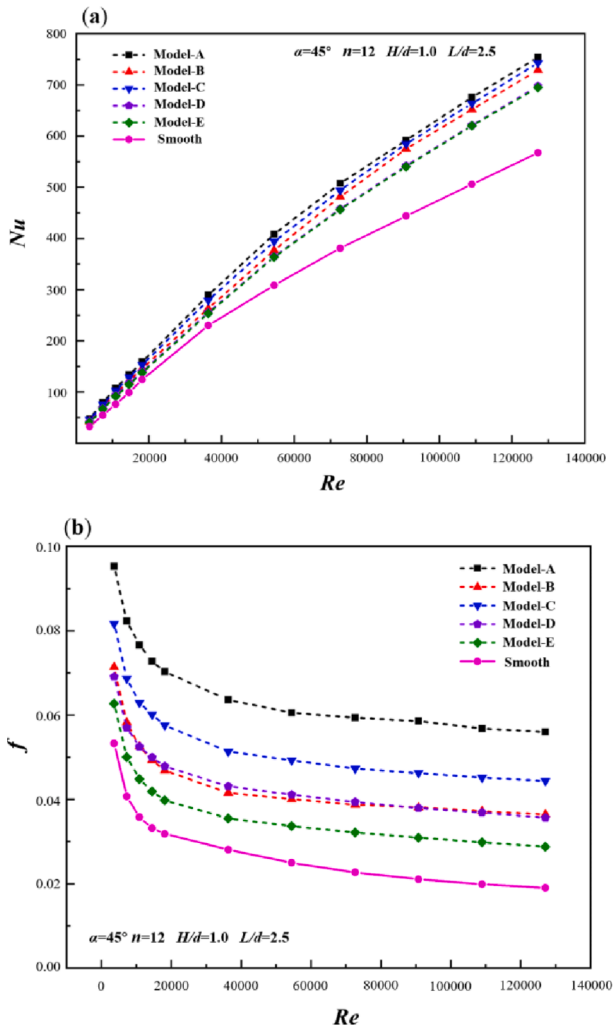


**Fig. 13.** Thermal–hydraulic parameters of different models at $\alpha = 45°$, $n = 12$, $H/d = 1.0$, and $L/d = 2.5$: (a)$Nu$ and (b) $f$.

Fig. 16 (a) that the cooling effect on the outer wall at $H/d = 1.0$ is second only to that at $H/d = 2.5$, which indicates that the cooling effect is jointly affected by both the heat transfer area and fluid disturbance.

The inner wall temperature of different $H/d$ with the $Wp$ are shown in Fig. 16 (b). It can be investigated that 0.5, 1.0 and 1.5 of $H/d$ can improve the cooling effect on the inner wall in the calculated $H/d$, while $H/d = 2.0$ and 2.5 reduce the inner cooling effect of DACTPS due to excessive blocking on fluid. $H/d = 0.5$ has a better inner cooling effect than $H/d = 1.0$, while the inner cooling effect of the smooth tube ($H/d = 0$) deteriorates. Thus, it is concluded that the $H/d$, which has the most significant improvement of a cooling effect on the inner wall is in the range of 0–1 when $\alpha$, $n$, and $L/d$ are constant at 45°, 12 and 2.5, respectively.

Fig. 17 shows the thermal–hydraulic parameters of different $H/d$ at $\alpha = 45°$, $n = 12$, and $L/d = 2.5$. It is indicated from Fig. 17 (a) that the $\Delta P$ increases sharply with $Re$. When $Re = 127000$, the $\Delta P$ of $H/d = 2.5$ is close to 20 kPa. Besides, the $\Delta P$ increases significantly with the $H/d$ increasing under the same $Re$. When $Re = 54000$, the $\Delta P$ of $H/d = 1.0$ reaches 2.1 kPa, only 55 % of that of $H/d = 2.5$. The $h$ rises by a small margin with the increase of $H/d$, as displayed in Fig. 17 (b). Fig. 17 (c) presents that the $EEC$ of $H/d = 0.5$ and 1.0 are in the range of 0.87–1.09 and 0.54–0.99 at the studied range of $Re$, respectively.

### 5.2.2. *Effects of the length–width ratio (L/d)*

In the present study, the performance of $L/d$ on heat transfer enhancement of discrete inclined ribs is investigated. Apparently, the length–width ratio can significantly influence the heat transfer enhancement of discrete inclined ribs because of the fluid disturbance effect and increased heat transfer area. Fig. 18 displays the temperature variations with different $L/d$ at $\alpha = 45°$, $n = 12$, and $H/d = 1.0$. It is visible that discrete inclined ribs with different $L/d$ enhance the outer cooling effect of DACTPS. The outer wall temperature of the smooth tube reaches 1500 K, while discrete inclined ribs reduce the outer temperature below 1300 K at $Re = 3600$, which is lower than the tolerable temperature of Inconel–625, as shown in Fig. 18 (a). Fig. 18 (b) presents the variations of the inner temperature with $Wp$ at $\alpha = 45°$, $n = 12$, and $H/d = 1.0$. It is revealed that discrete inclined ribs with different $L/d$ reduce the inner temperature significantly at the same $Wp$. In the calculated $L/d$, $L/d = 1.5$ has the minimum inner wall temperature, while the inner temperature of $L/d = 1.0$ and 2.0 increase at the same $Wp$. Therefore, it can be concluded that the best $L/d$ value for inner wall cooling is between 1.0 and 2.0 when $\alpha$, $n$ and $H/d$ are constant at 45°, 12, and 1.0, respectively.

Fig. 19 displays the thermal–hydraulic parameters of different $L/d$ with $Re$ at $\alpha = 45°$, $n = 12$, and $H/d = 1.0$. From Fig. 19 (a), with the increase of $L/d$, the $\Delta P$ increases accordingly. The $\Delta P$ of $L/d = 4.0$ reaches 12 kPa, while the $\Delta P$ of $L/d = 1.5$ is only 6.5 kPa at $Re = 127000$. Moreover, with the increase of $\Delta P$, the disturbance effect of discrete inclined ribs is more pronounced, and the $h$ increases, as shown in Fig. 19 (b). It is found from Fig. 19 (c) that the $EEC$ of $L/d = 1.5$ is 0.85–1.05 at the studied $Re$, which means overly better thermal–hydraulic performance than the smooth tube.

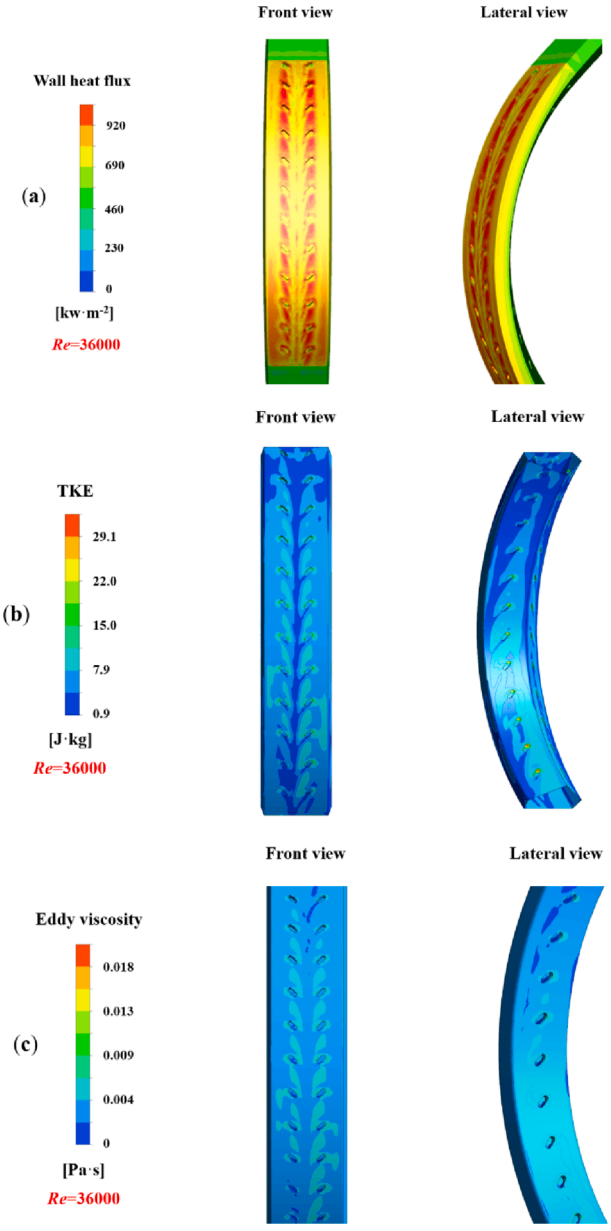


**Fig. 14.** Thermal–hydraulic performance contour of model D at $\alpha = 45°$, $n = 12$, $H/d = 1.0$, and $L/d = 2.5$: (a) Wall heat flux, (b) TKE and (c) Eddy viscosity.

### 5.2.3. *Effects of group number of ribs (n)*

The thermal–hydraulic performance of different group numbers of ribs ($n$) at $\alpha = 45°$, $L/d = 2.5$, and $H/d = 1.0$ is investigated to confirm the best $n$. The variations of temperature with different $n$ are illustrated in Fig. 20. It is visible that discrete inclined ribs can significantly improve the cooling effect on the outer wall. The DACTPS with discrete inclined ribs can decrease the outer wall temperature below 1250 K at the same $Re$, as shown in Fig. 20 (a). Fig. 20 (b) presents the inner wall temperature of different $n$ with $Wp$ at $\alpha = 45°$, $L/d = 2.5$ and $H/d = 1.0$. At the same $Wp$, the channel with $n = 7$ has the best cooling effect on the inner wall, as represented by the pink line in Fig. 20 (b).

To analyze thermal–hydraulic and hydrodynamic performance of DACTPS with different $n$ at $\alpha = 45°$, $L/d = 2.5$ and $H/d = 1.0$, three parameters are depicted in Fig. 21. It can be seen from Fig. 21 (a) that the $\Delta P$ increases with the increase of $n$. Compared with the results of the smooth tube, the $\Delta P$ increases by 17.7 %–57.3 % at $n = 7$ and increases by 34.7 %–103.6 % at $n = 15$ as the $Re$ varies in 3600–127000. Fig. 21 (b) shows the effects of the group number $n$ on $h$. It is noteworthy that

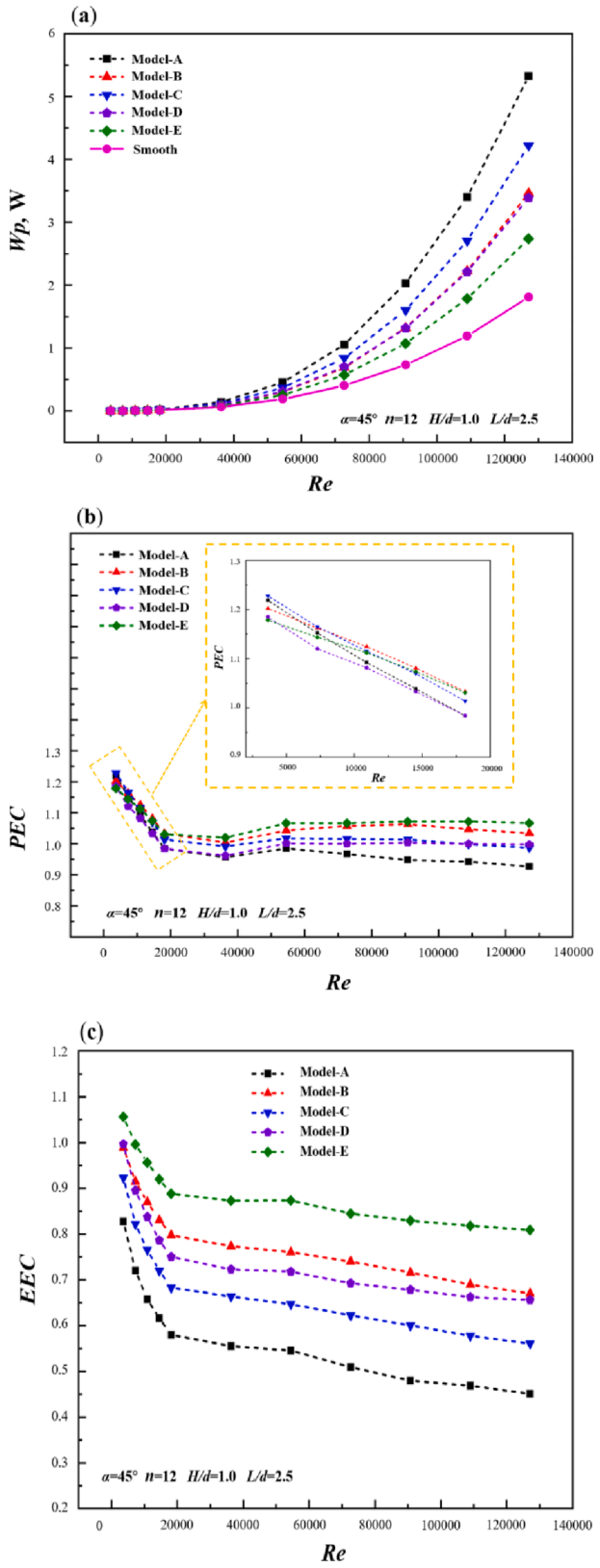


**Fig. 15.** Variations of thermal–hydraulic performances with $Re$ of different models at $\alpha = 45°$, $n = 12$, $H/d = 1.0$, and $L/d = 2.5$: (a) $Wp$, (b) $PEC$ and (c) $EEC$.

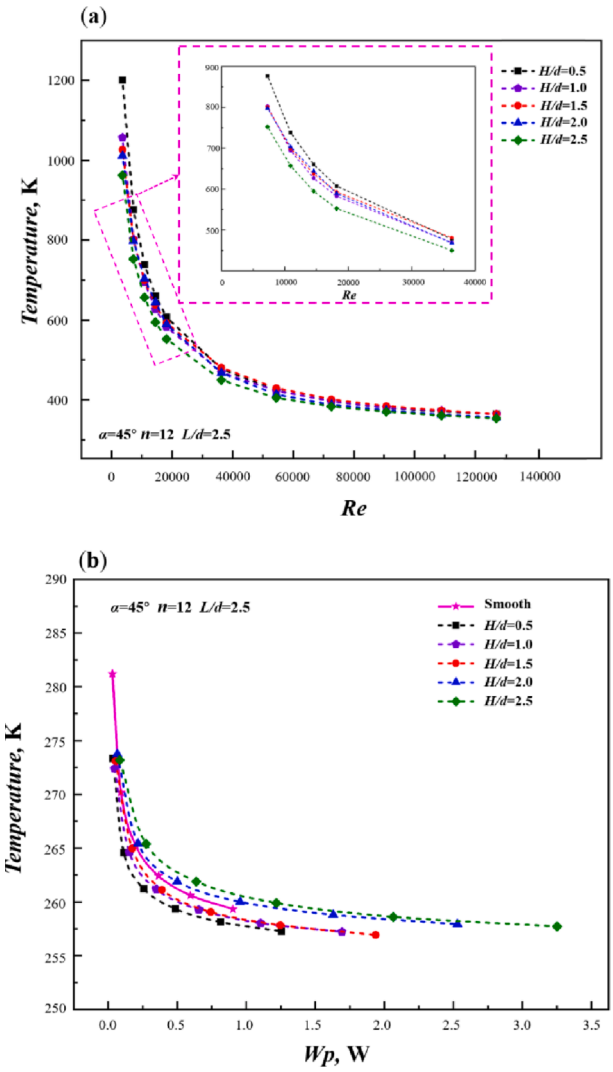


**Fig. 16.** Variations of temperature of different $H/d$ at $\alpha = 45°$, $n = 12$, and $L/d = 2.5$: (a) outer wall and (b) inner wall with $Wp$.

the $h$ of different $n$ has less difference basically, while increases obviously compared with the $h$ of the smooth tube. With the addition of $n$, the heat transfer area increases, leading to a greater heat transfer performance. So the outer temperature of $n = 15$ is the lowest in Fig. 20 (a). However, the inner temperature depends not only on the heat transfer area but also on the disturbance of the flow field. Fig. 21 (c) displays the variation of $EEC$ with $Re$ at $\alpha = 45°$, $L/d = 2.5$ and $H/d = 1.0$. The $EEC$ of $n = 7$ ranges from 0.78 to 1.04, with $Re$ varies in 3600–127000.

In order to better analyze the reason for the excellent inner wall cooling effect of the enhanced bend tube with $n = 7$, Fig. 22 presents the streamline and tangential vector graph with $n = 0$, $n = 15$ and $n = 7$ at $Re = 18000$. It is investigated that multiple pairs of longitudinal swirls are generated by secondary circulation and discrete inclined ribs, as shown in Fig. 22 (b) and (c). Longitudinal swirls form circulation between the near wall and internal fluid, which improves heat transfer performance. However, compared with the result of $n = 15$, $n = 7$ has two pairs of longitudinal swirls near the inner wall, as displayed by the red circle in Fig. 22 (b). $n = 15$ has an excessive restriction on longitudinal swirls in fluid, which leads to the disappearance of small vortexes near the wall.

### 5.2.4. Effects of the tilt angle ($\alpha$)

As one of the influencing parameters of thermal–hydraulic and thermodynamic performance of discrete inclined ribs enhanced bend

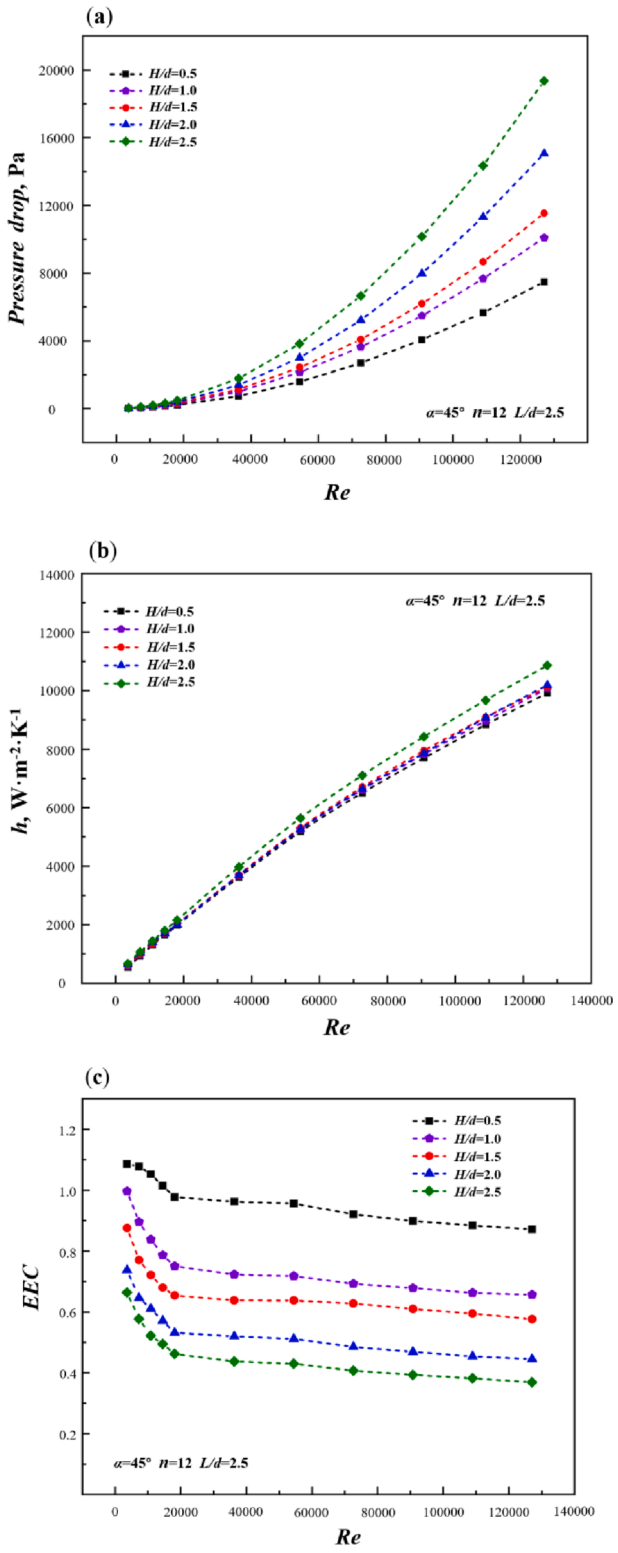


**Fig. 17.** Thermal–hydraulic parameters of different $H/d$ at $\alpha = 45°$, $n = 12$, and $L/d = 2.5$: (a) $\Delta P$, and (b) $h$, and (c) $EEC$.

tube, the effects of the tilt angle ($\alpha$) are investigated in the present study. Fig. 23 shows the temperature variations with different $\alpha$ at $n = 7$, $L/d = 2.5$ and $H/d = 1.0$. At low $Re$, the outer temperature of the enhanced bend tube is obviously lower than that of the smooth tube at different $\alpha$, while at high $Re$, due to the different turbulence effects caused by the $\alpha$, the outer wall temperature at $\alpha = 60°$ and 75° are higher than that of the

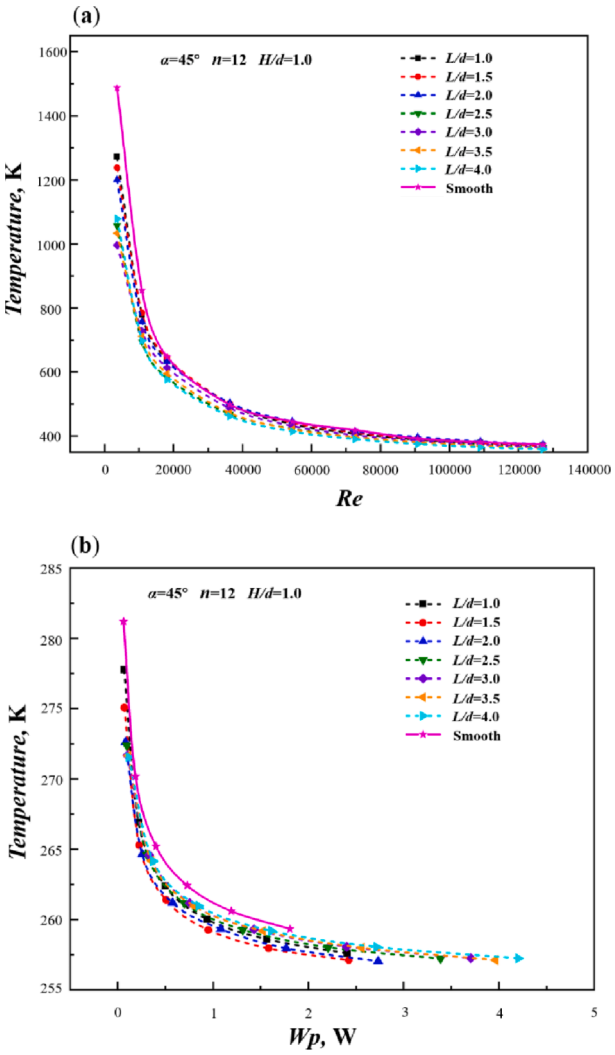


**Fig. 18.** Variations of temperature with different $L/d$ at $\alpha = 45°$, $n = 12$, and $H/d = 1.0$: (a) outer wall and (b) inner wall with $Wp$.

smooth tube, which has little impact on hypersonic aircraft because the outer wall temperature is far below the tolerance temperature of solid material, as depicted in Fig. 23 (a). Moreover, Fig. 23 (b) presents the variations of the inner temperature with $Wp$ of different $\alpha$ at $n = 7$, $L/d = 2.5$ and $H/d = 1.0$. Under the same $Wp$, the cooling effect of different $\alpha$ on the inner wall is better than that of the smooth tube, and $\alpha = 15°$ has the best cooling effect on the inner wall in all studied $\alpha$. It is worth emphasizing that the inner wall temperature of $\alpha = 15°$ and $Wp = 2.24$ W is as low as 256.9 K, which is lower than that of $\alpha = 45°$ and $Wp = 2.8$ W.

In order to investigate thermal–hydraulic performance of discrete inclined ribs with different $\alpha$ at $n = 7$, $L/d = 2.5$ and $H/d = 1.0$, the variations of thermal–hydraulic parameters with $Re$ are presented in Fig. 24. Fig. 24 (a) shows that the smooth tube has the minimum $\Delta P$, while the $\Delta P$ of $\alpha = 15°$ is lower than that of $\alpha = 0°$. It is indicated that $\alpha = 15°$ is the most suitable turbulence direction for secondary circulation in bend tube in all studied $\alpha$, leading to the trend of $\Delta P$ in Fig. 24 (a). Compared with the smooth tube, the $Nu$ of different $\alpha$ increase significantly, as depicted in Fig. 24 (b). It can be obtained from Fig. 24 (c) that the distribution regularity of $EEC$ of different $\alpha$ is not apparent at lower $Re$, while $\alpha = 15°$ has the maximum $EEC$ of all studied $\alpha$ when the disturbance formed by the discrete inclined ribs and the secondary circulation develops ultimately at higher $Re$.

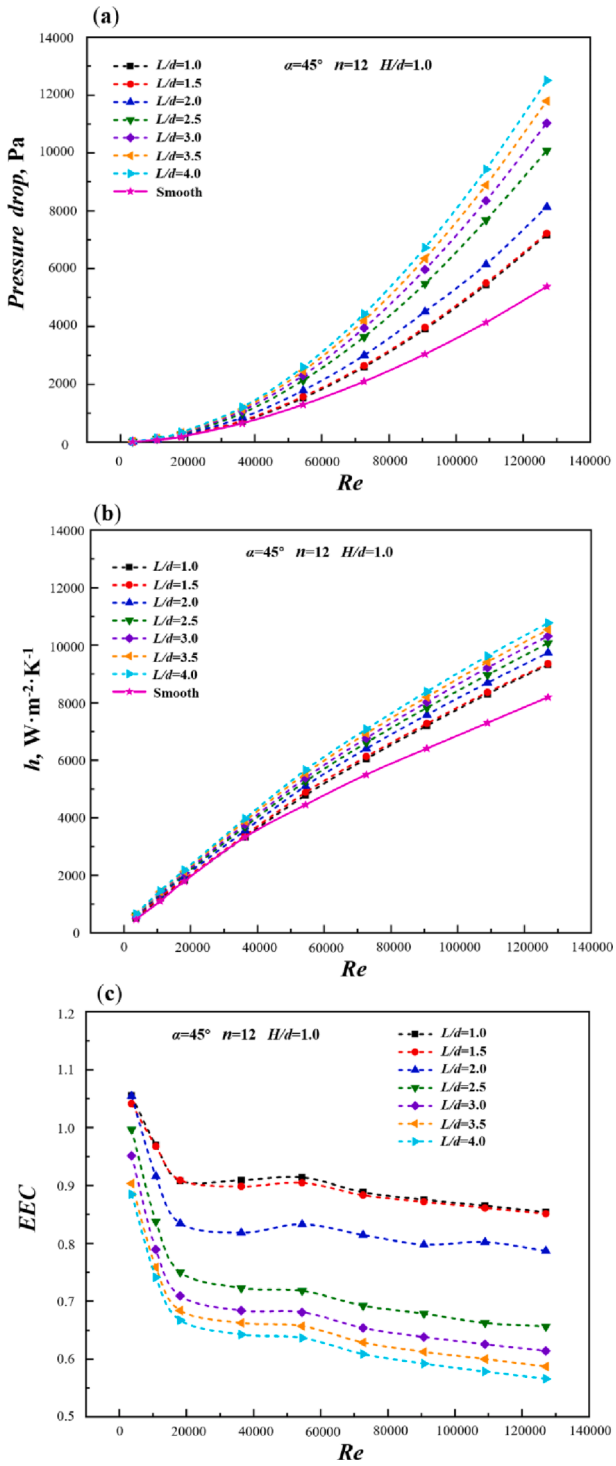


**Fig. 19.** Thermal–hydraulic parameters of different $L/d$ at $\alpha = 45°$, $n = 12$, and $H/d = 1.0$: (a) $\Delta P$, (b) $h$ and (c) $EEC$.

## 6. Optimization of discrete inclined ribs parameters

### 6.1. Optimization procedure

The direct heat conduction problem is solved using the CFD software above, as shown in Sections 5.1 and 5.2. The effects of $H/d$, $L/d$, $n$ and $\alpha$ are studied, respectively. However, the synergistic effect is not considered while the geometric parameters are changing simultaneously. It is unreliable to obtain the optimal solution based solely on the parametric

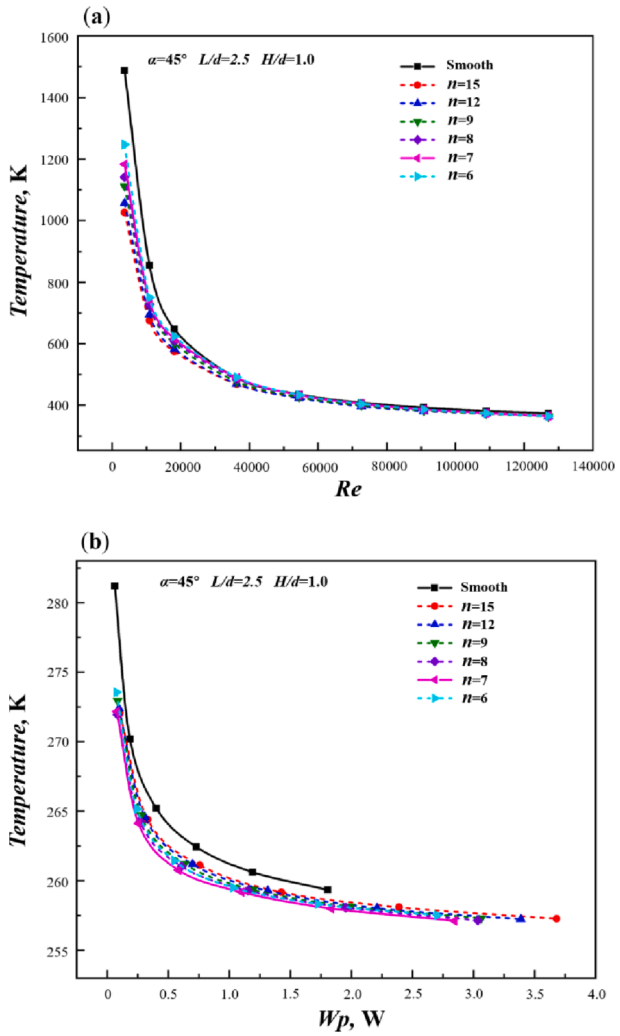


**Fig. 20.** Variations of temperature with different $n$ at $\alpha = 45°$, $L/d = 2.5$, and $H/d = 1.0$: (a) outer wall and (b) inner wall with $Wp$.

analysis in Section 5.2. Therefore, it is essential to use a professional optimization algorithm for overall optimization.

The $H/d$, $L/d$, $n$ and $\alpha$ are considered primary design variables and determining factors for the comprehensive active cooling thermal protection performance of the discrete inclined ribs enhanced bend tube. It should be pointed out that the difference between design variables and working conditions. The parameters such as $H/d$, $L/d$, $n$ and $\alpha$ are difficult to change after the design of ACTPS is determined. These parameters are regarded as variables in the optimization process. But for $Re$, when hypersonic aircraft is heated by different heat fluxes, the active thermal protection requirements are met by changing $Re$ or inlet velocity, which is called working condition change. It can be found in Section 5 that the size relationship of overall thermal–hydraulic performance such as $T_{in}$, $\Delta P$ and $EEC$ of ACTPS with different variables are not changed by the increase of $Re$. Therefore, we carry out the optimization process of variables under the same $Re = 72000$. The obtained optimal solution will have better active thermal protection performance under a more extensive range of $Re$. And the same method has been used to obtain the optimal solution of variables in many references [32,52]. For the inlet temperature, it also can be found that the size relationship of the overall thermal–hydraulic performance of ACTPS with different variables is not changed by the change of the inlet temperature [39]. Moreover, if RP-3 is used as the cooling medium, its inlet temperature is certain before preheating by the ACTPS. So, the $Re$ and inlet temperature are not considered design variables for ANN.

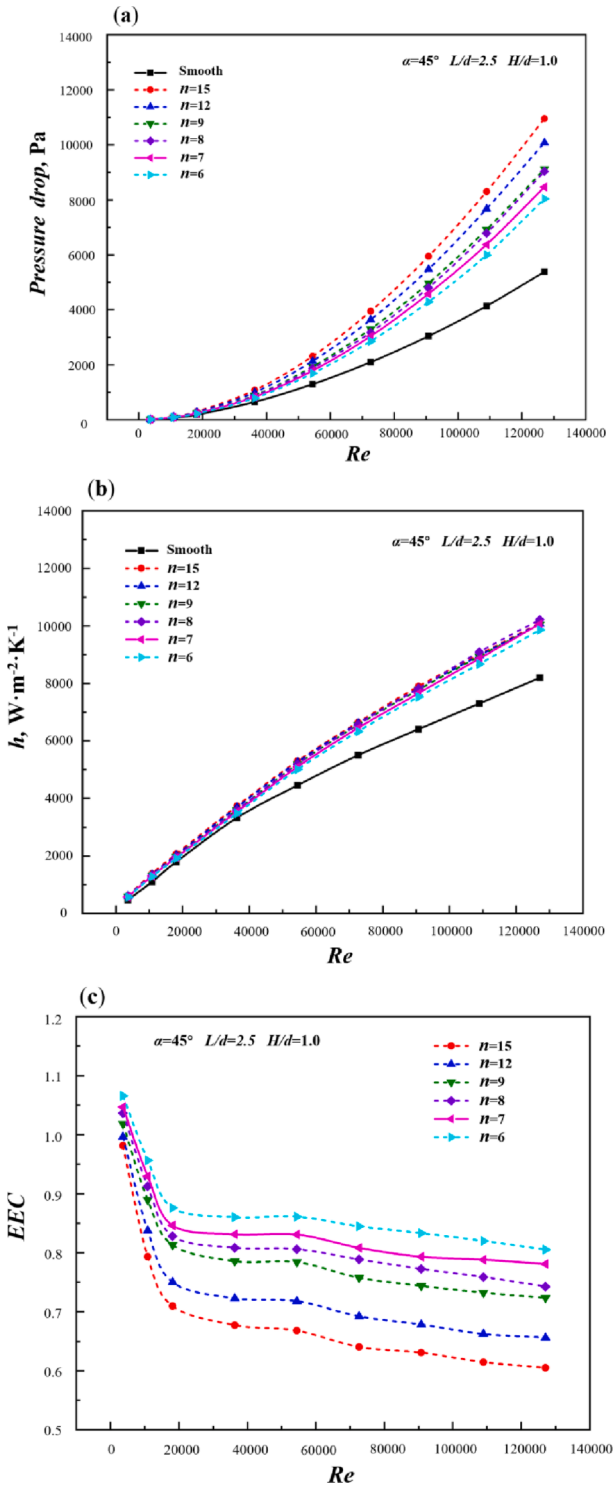


**Fig. 21.** Thermal–hydraulic parameters of different $n$ at $\alpha = 45°$, $L/d = 2.5$, and $H/d = 1.0$: (a) $\Delta P$, (b) $h$, and (c) $EEC$.

When the outer wall of hypersonic aircraft is heated by high heat flux, the work of ACTPS is to control the inner wall temperature ($T_{in}$) within a certain range to ensure the normal operation of the internal electronic devices. Therefore, reasonable $T_{in}$ is the object of our optimization. It is noteworthy that the comprehensive index $EEC$ or $PEC$ may not be optimal under the optimal $T_{in}$. Under the target of controlling the $T_{in}$, the smaller the pressure drop ($\Delta P$), the less the pump power consumed, and the more obvious the advantages of the ACTPS. The $T_{in}$ and $\Delta P$ are determined as two conflicting objectives, which represent

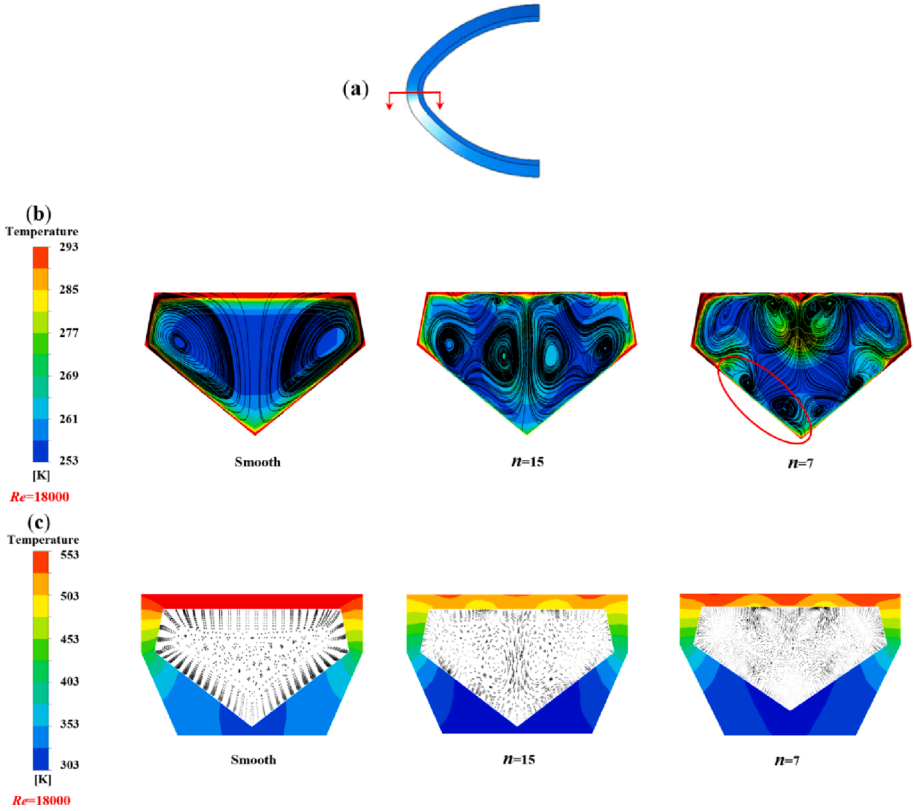


**Fig. 22.** Streamline and tangential vector graph of enhanced bend tube with $n = 0$, $n = 15$, and $n = 7$ at $Re = 18000$: (a) section location, (b) streamline, and (c) tangential vector.

the thermal protection performance and the flow resistance separately. In view of the heavy workload of direct optimization of the CFD method, the ANN is adopted as a surrogate model to express the relationship between the design variables and objectives. [32] The networks for the $T_{in}$ and $\Delta P$, which are trained by ANN, are applied as the objective functions. Multi–objective optimization is realized using Genetic Algorithm (GA) in MATLAB. Finally, the optimal Pareto front is solved, and the optimal solutions are determined according to corresponding evaluation criteria. [52] The optimization procedure is illustrated in Fig. 25.

### 6.2. Orthogonal experimental design

The number of tests will increase exponentially if full–factor numerical simulation is applied to explore the optimal parameters. The orthogonal experimental design can reduce the number of tests while having the advantages of neat comparability and uniform dispersion. [53] Table 4 presents the orthogonal experimental design scheme, named $L_9$ ($3^4$), which consists of four variables ($H/d$, $L/d$, $n$, and $\alpha$) with three levels, respectively. Table 4 is used to analyze range (ANOR) [54] to investigate the primary and secondary order and significance of the influence of four factors.

Table 5 and 6 present the ANOR results of two criteria, $T_{in}$ and $\Delta P$, respectively. The calculating equations are as follows [55]:

$$R = max\{I_j, II_j, III_j\} - min\{I_j, II_j, III_j\} \tag{20}$$

where $I_j$, $II_j$ and $III_j$ are the sum of criterion corresponding to j column factors at levels 1, 2 and 3, respectively. For example, the data related to $I_j$ and $H/d$ in Table 5 is 785.72, which is the sum of three data 263.07, 261.19, 261.46 in Table 4. These three data are the corresponding $T_{in}$ orthogonal experimental results when $H/d$ is 0.5. Similarly, the data related to $III_j$ and $L/d$ in Table 6 is 11370.88, which is the sum of three data 2894.70, 4311.60, 4164.58 in Table 4. These three data are the corresponding $\Delta P$ orthogonal experimental results when $L/d$ is 3.5. The size of range $R$ reflects the effect of related factors on the criterion, as shown in Tables 5 and 6.

It can be obtained that the order of $R_T$ from large to small is $L/d$, $\alpha$, $n$ and $H/d$, which means that the change of the factor $H/d$ has the most minor influence on the $T_{in}$, while the order of $R_P$ from large to small is $H/d$, $\alpha$, $n$ and $L/d$, which means that the change of the factor $H/d$ has the greatest influence on the $\Delta P$. Moreover, the ANOR results of the factor $H/d$ observed to be identical with the parametric analysis results in Section 4.2.1. The enhanced bend tube with $H/d = 0.5$ has the lowest $T_{in}$ at the same $Wp$, as depicted in Fig. 16 (c). It can be concluded that factor $H/d$ increases the $\Delta P$ significantly while having little effect on $T_{in}$. Videlicet, in the process of increasing the variable $H/d$, more pump power is consumed, but the little cooling benefit is obtained. As shown in Tables 5 and 6, factor $L/d$ can cause a significant variation in $T_{in}$ at a lower $\Delta P$ cost, and the effects of the factor $\alpha$, $n$ on $T_{in}$ and $\Delta P$ are moderate. Consequently, the factor $H/d$ is fixed at 0.5 mm in the follow–up study.

### 6.3. Results of ANNs

As listed in Table 7, The values of three design variables are uniformly selected for CFD simulation. Regarding the rule of the orthogonal test, an orthogonal experimental design scheme, named $L_{49}$ ($7^3$), consists of three design variables ($L/d$, $n$, and $\alpha$) with 7 levels, respectively. The CFD results of 49 cases are used as sample data for the ANN.

A three-layer back propagation ANN with a tan–sigmoid transfer functions at hidden and output layers is applied to train the data derived from numerical simulations [52]. ANN contains an input layer with three neurons ($L/d$, $n$, and $\alpha$), a hidden layer and an output with one neuron ($\Delta P$ or $T_{in}$), as depicted in Fig. 26. Subsequently, Fig. 27 illustrates the neuron-independent test in the hidden layer. The Mean Square Error (*MSE*) and Regression coefficient (*Reg*) are used as the evaluation

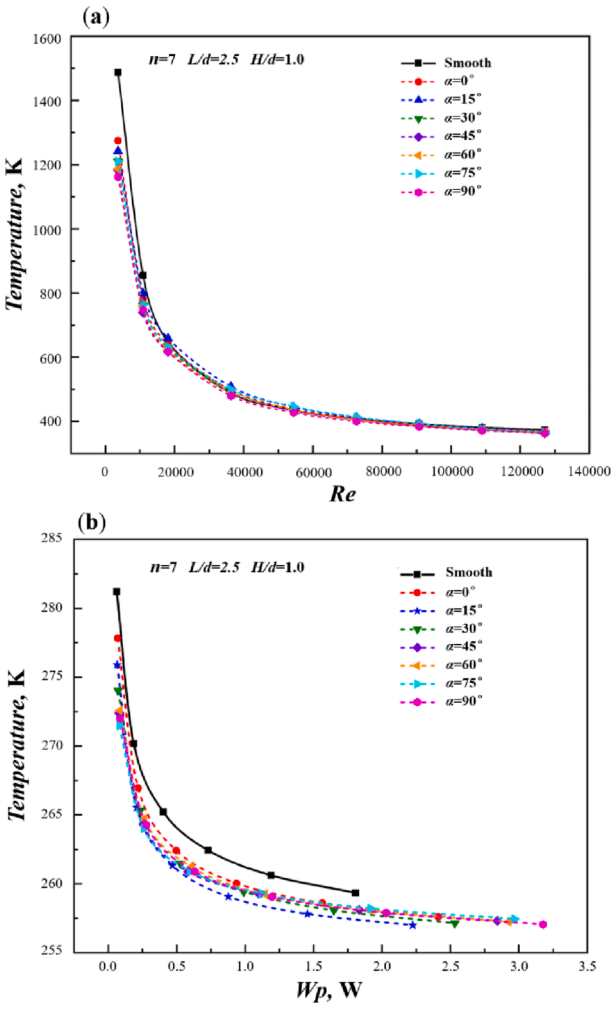


**Fig. 23.** Variations of temperature with different $\alpha$ at $n = 7$, $L/d = 2.5$, and $H/d = 1.0$: (a) outer wall and (b) inner wall with $Wp$.

indexes of the training results. They are expressed as follows: [56–58]

$$MSE = \frac{1}{N}\sum_{i=1}^{N}(y_i - y_{i,ANN})^2 \tag{21}$$

$$Reg = \sqrt{\frac{\sum_{i=1}^{N}(y_{i,ANN} - \bar{y})^2}{\sum_{i=1}^{N}(y_i - \bar{y})^2}} \tag{22}$$

The number of neurons in the hidden layer affects the accuracy of the ANN. [51] Smaller *MSE* and *Reg* close to 1 lead to higher prediction accuracy, so hidden layers of 8 and 9 neurons are chosen in the study for $\Delta P$ and $T_{in}$, respectively.

Random 80 % and 20 % of data are used for network training and testing, respectively. In the prediction process of ANN, 80 % of calculated CFD results are used for neural network training, and the remaining 20 % are used to test the trained neural network to improve its prediction accuracy. Fig. 28 compares the values of CFD results and values of ANN prediction. The maximum relative error of the pressure drop $\Delta P$ is + 2.6 % and −4.7 %, +0.21 % and −0.28 % of the maximum inner wall temperature $T_{in}$. Based on the above, ANN has a relatively reliable prediction accuracy.

### 6.4. Results of multi–objective optimization

In the present study, the general feature of heat transfer enhancement is that the $T_{in}$ decreases with the increase of $\Delta P$. The

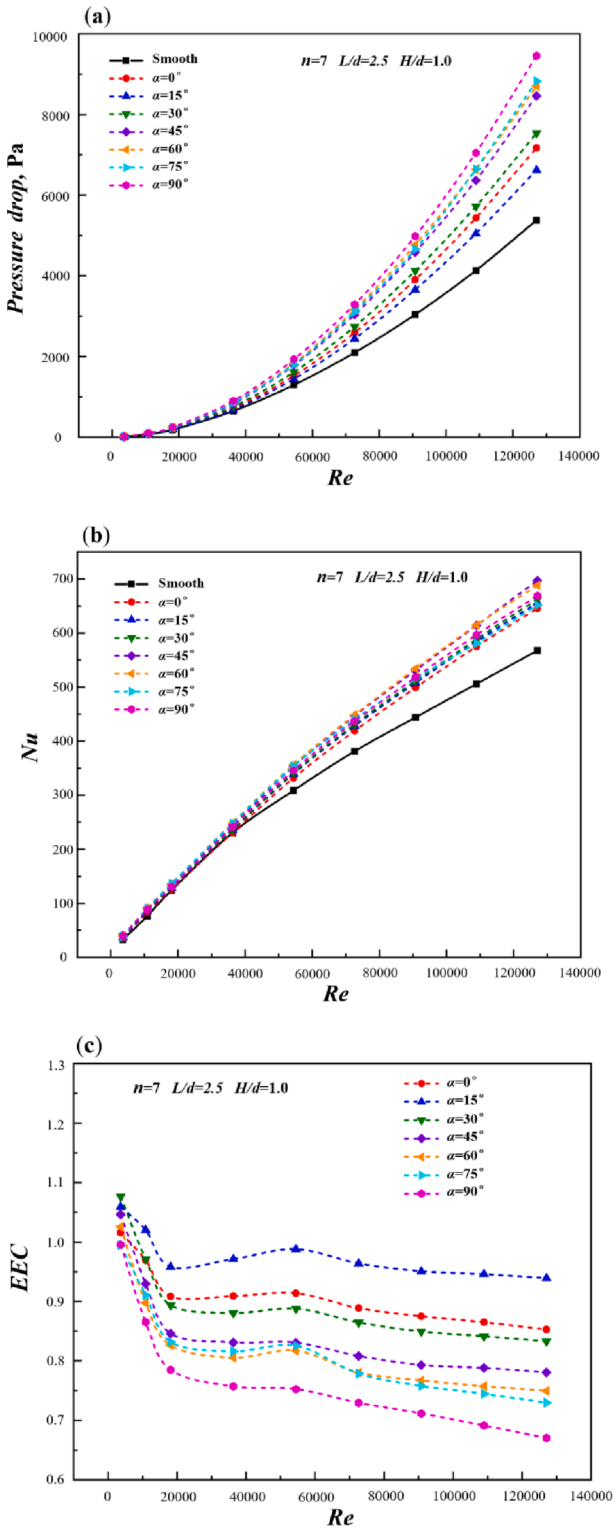


**Fig. 24.** Thermal–hydraulic parameters of different $\alpha$ at $n = 7$, $L/d = 2.5$, and $H/d = 1.0$: (a) $\Delta P$, (b) $Nu$, and (c) $EEC$.

multi–objective optimization problem can be expressed as follows:

$$\begin{aligned} &\text{Minimization} \quad \Delta P = net_{\Delta P}(L/d,\ n,\ \alpha) \\ &\qquad\qquad T_{in} = net_{T_{in}}(L/d,\ n,\ \alpha) \\ &\text{Subject} \quad L/d \in [1.0,\ 4.0] \end{aligned} \tag{23}$$

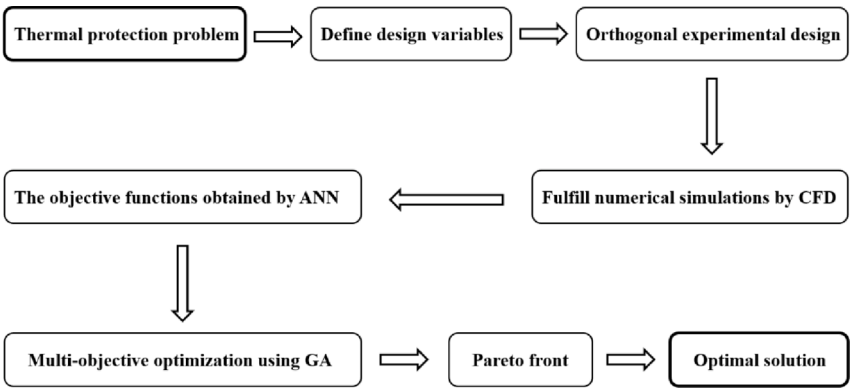


**Fig. 25.** The multi–objective optimization procedure of design variables.

**Table 4**
Orthogonal experimental design scheme and results.

| Test number | *H/d* | *L/d* | *n* | *α* | $T_{in}$ | Δ*P* |
|---|---|---|---|---|---|---|
| 1 | 1 (0.5) | 1 (1.5) | 1 (7) | 1 (15) | 263.07 | 2201.79 |
| 2 | 1 (0.5) | 2 (2.5) | 3 (12) | 2 (45) | 261.19 | 2694.14 |
| 3 | 1 (0.5) | 3 (3.5) | 2 (9) | 3 (75) | 261.46 | 2894.70 |
| 4 | 2 (1.5) | 1 (1.5) | 3 (12) | 3 (75) | 263.25 | 3578.11 |
| 5 | 2 (1.5) | 2 (2.5) | 2 (9) | 1 (15) | 261.00 | 2902.13 |
| 6 | 2 (1.5) | 3 (3.5) | 1 (7) | 2 (45) | 260.97 | 4311.60 |
| 7 | 3 (2.5) | 1 (1.5) | 2 (9) | 2 (45) | 261.17 | 4334.53 |
| 8 | 3 (2.5) | 2 (2.5) | 1 (7) | 3 (75) | 262.65 | 6128.73 |
| 9 | 3 (2.5) | 3 (3.5) | 3 (12) | 1 (15) | 261.40 | 4164.58 |

**Table 5**
ANOR results of $T_{in}$.

| Results | *H/d* | *L/d* | *n* | *α* |
|---|---|---|---|---|
| $I_j$ | 785.72 | 787.49 | 786.69 | 785.47 |
| $II_j$ | 785.22 | 783.36 | 783.63 | 783.33 |
| $III_j$ | 785.22 | 783.83 | 785.84 | 787.36 |
| $R_T$ | 0.50 | 4.13 | 3.06 | 4.03 |

**Table 6**
ANOR results of Δ*P*.

| Results | *H/d* | *L/d* | *n* | *α* |
|---|---|---|---|---|
| $I_j$ | 7790.63 | 10114.43 | 12642.12 | 9268.5 |
| $II_j$ | 10791.84 | 11725.00 | 10131.36 | 11340.27 |
| $III_j$ | 14627.84 | 11370.88 | 10436.83 | 12601.54 |
| $R_P$ | 6837.21 | 1610.57 | 2510.76 | 3333.04 |

**Table 7**
Selected values of design variables for CFD.

| Variables | Values |
|---|---|
| *L/d* | 1.0, 1.5, 2.0, 2.5, 3.0, 3.5, 4.0 |
| *n* | 6, 7, 8, 9, 10, 11, 12 |
| *α*/° | 0, 15, 30, 45, 60, 75, 90 |

$$n \in [6,\ 15]$$

$$\alpha \in [0^{\circ},\ 90^{\circ}] \tag{24}$$

The group number of ribs *n* must be integral to the actual conditions. Therefore, it is rounded in the optimization process. It is pointed out that the minimum change of *L/d* and *α* are 0.5 and 15° to facilitate production in general engineering applications. The theoretical optimal solution and engineering optimal solution will be given in the following research, respectively. A non-dominated sorting genetic algorithm (NSGA-II) [59] is applied for multi–objective optimization to get the Pareto front. Table 8 shows the parameter settings of NSGA-II. The Pareto front is obtained as depicted in Fig. 29.

The Technique for Order Preference by Similarity to Ideal Solution (TOPSIS) was developed by Yoon and Hwang [60]. The idea of TOPSIS is to evaluate the comprehensive distance between any scheme in the system and the ideal and negative ideal optimal solution through calculation, which are represented by O and O' in Fig. 29, separately. The relative closeness to the ideal solution represented by the evaluation index, which is also depicted in Fig. 29. It is investigated that point B has the highest value of *C* in the optimization range. Therefore, the individual marked by point A, at which the *L/d*, *n*, and *α* are equal to 3.19, 11 and 14.3°, is the optimal solution chosen by TOPSIS. However, in practical engineering, the design variables corresponding to the optimal solution are approximately 3, 11 and 15°, respectively. The values of objectives for the optimal solution point A are 261.86 K and 2471.2 Pa. Compared with the smooth tube, the Δ*P* only increases by 375.5 Pa, about 18 %. At the same time, the inner wall temperature decreases by 3.36 K, which means a significant improvement in the cooling performance of DACTPS for hypersonic aircraft. Meanwhile, the geometric model of point A is simulated to get $EEC = 1.02$, and $PEC = 1.09$ at $Re = 72000$, which is in a fully turbulent flow state. Point A achieves an excellent cooling effect and thermal–hydraulic performance with moderate pressure drop. It is proved that discrete inclined ribs enhanced bend tube based on DACTPS is a potential thermal protection structure for hypersonic aircraft and has excellent synthetically cooling performance. Moreover, it should be considered to be applied in other turbulence thermal protection problems to improve thermal–hydraulic performance and reduce energy consumption.

In order to verify the effect of optimization and the accuracy of ANN prediction, the CFD results of design variables for Point A are given in different *Re*, as depicted in Fig. 30 and Fig. 31, respectively. Fig. 30 presents the variations of the $T_{in}$ with *Wp* of the smooth tube and optimized tube. With the increase of *Wp*, the $T_{in}$ of the smooth tube and optimized tube decreases significantly. However, the curve of the optimized tube is located below the curve of the smooth tube, which means that the cooling effect of the optimized tube is better than the smooth tube under the same *Wp*. Fig. 31 (a) and (b) show the variations of the Δ*P* and $T_{in}$ with *Re* of the optimized tube. It can be found from Fig. 31 (b) that when the *Re* reaches 20000, the $T_{in}$ of the optimized ACTPS can be reduced to below 300 K. Moreover, When $Re = 72000$, the CFD results of Δ*P* and $T_{in}$ are 2416.4 Pa and 261.62 K, respectively. The deviation of Δ*P* and $T_{in}$ prediction results of ANN for the corresponding design variables of point A is 2.3 % and 0.09 %, respectively. The 49 sets of CFD results selected by orthogonal experimental design form an ANN with high prediction accuracy.

It is found from CFD results of Point A that discrete inclined ribs enhanced bend tube in the present study has a good thermal–hydraulic

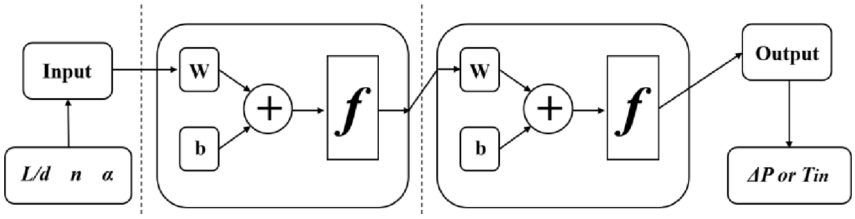


**Fig. 26.** Schematic of a three-layer neural network.

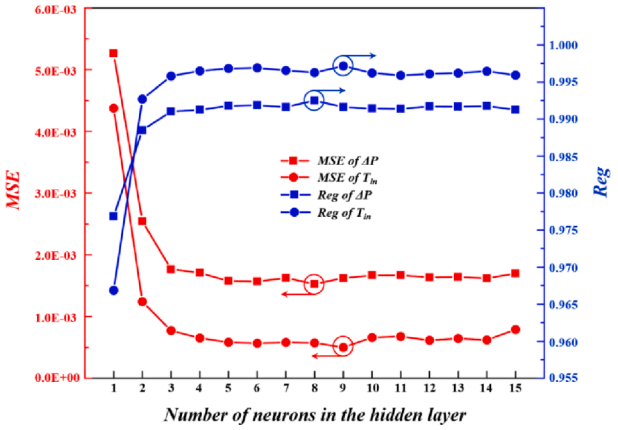


**Fig. 27.** Neuron independence test.

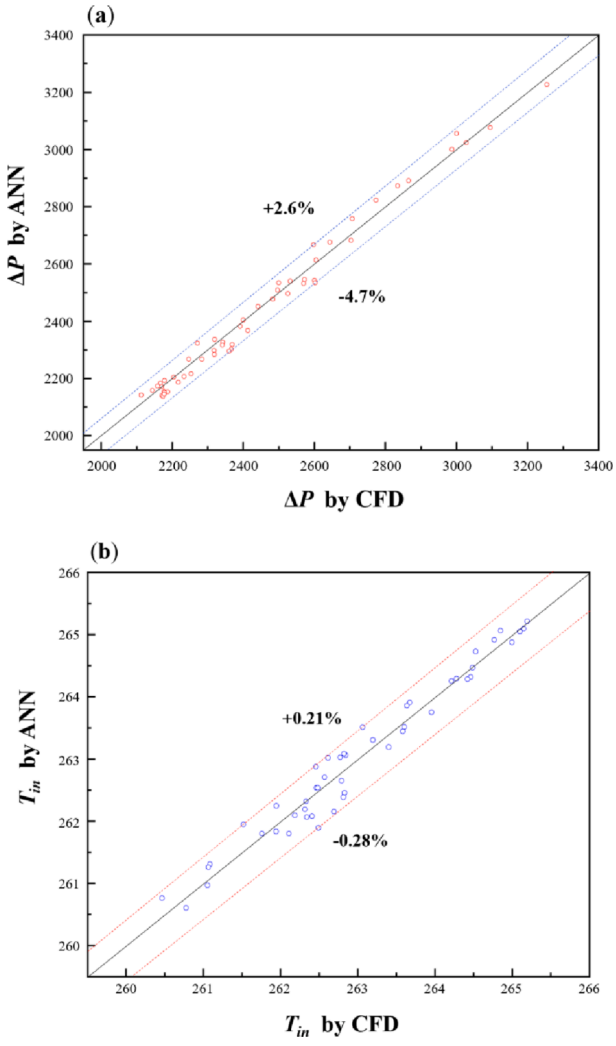


**Fig. 28.** The relative error of CFD simulation and ANN prediction: (a) $\Delta P$ and (b) $T_{in}$.

performance at larger *Re* range. Comparisons between the present study and references are presented in Fig. 32. The enhanced heat transfer components under lower *Re* are selected as wavy delta winglet [61], conical protrusion [62], inclined trapezoidal vortex generators [48], perforated trapezoidal winglet [63], punched rectangular wing [64] and V-baffles [65]. And the compared works under higher *Re* are inserting inclined curved-twisted baffles [66], plate inserts [67], longitudinal fins with Nano fluid [68], corrugated tube [69], inserting rods [70], straight tube with ribs [71] and conical strip inserts [40]. As shown in Fig. 32, discrete inclined ribs enhanced bend tube has an excellent thermal–hydraulic performance at a larger *Re* range. With the increase of *Re*, the *EEC* decreases slowly and stabilizes near 1.0. Moreover, it is worth noting that the enhanced bend tube realizes a coupling mechanism of flow and heat transfer enhancement. The secondary circulation generated by the leading edge curvature of hypersonic aircraft and longitudinal swirls generated by the discrete inclined ribs cooperate to achieve heat transfer enhancement with higher overall thermal–hydraulic performance, thereby improving the active cooling performance of DACTPS for hypersonic aircraft.

## 7. Conclusions

In the present study, a discrete inclined ribs enhanced bend tube based on "Diamond" active cooling thermal protection system (DACTPS) for hypersonic aircraft was proposed. The thermal–hydraulic and active cooling effects were investigated through numerical simulation. Meanwhile, the impact of different parameters, including rib height–width ratio ($H/d$), length–width ratio ($L/d$), group number of ribs ($n$) and tilt angle ($\alpha$) combined with their heat transfer enhancement mechanism, were analyzed. The conclusions are summarized as follows:

(1) The discrete inclined ribs enhanced bend tube realizes a coupling mechanism of flow and heat transfer enhancement. The secondary circulation generated by the bend tube and longitudinal swirls generated by the discrete inclined ribs cooperate to achieve heat transfer enhancement with higher overall thermal–hydraulic performance, thereby improving the active cooling performance of ACTPS for hypersonic aircraft.

(2) Five different arrangements of ribs are designed and investigated. The *Nu* of the enhanced bend tubes are 22 %–33 % higher than

**Table 8**
Parameter settings of NSGA-II.

| Parameters | Values |
|---|---|
| Population size | 300 |
| Generations | 1000 |
| Crossover fraction | 0.8 |
| Pareto fraction | 0.3 |
| Functional tolerance | 1E-5 |

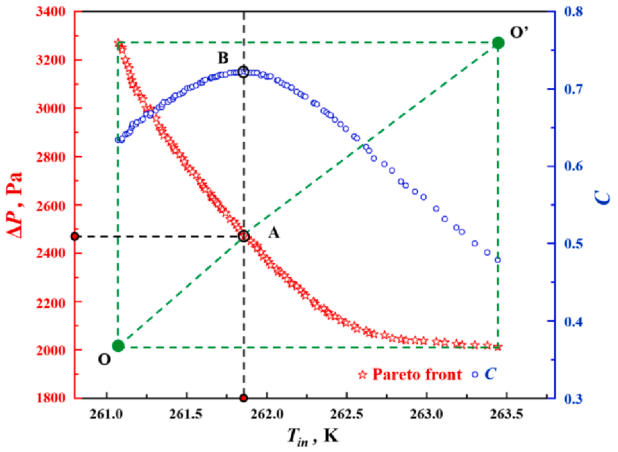


**Fig. 29.** Pareto front for $\Delta P$ and $T_{in}$.

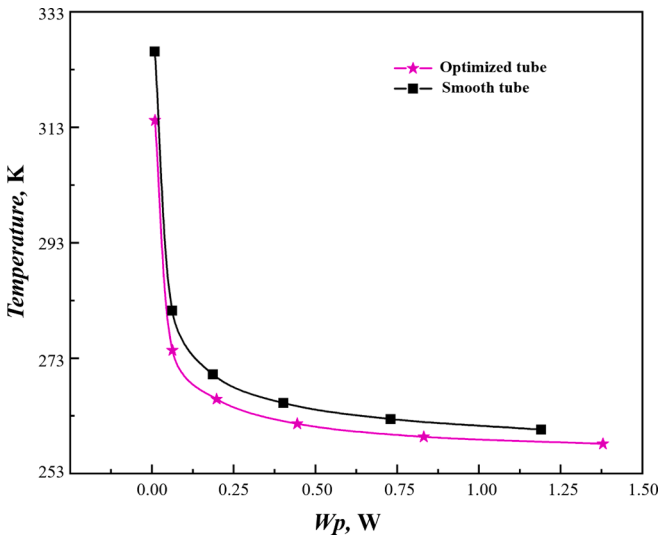


**Fig. 30.** Variations of $T_{in}$ with different $Wp$ of smooth tube and optimized tube.

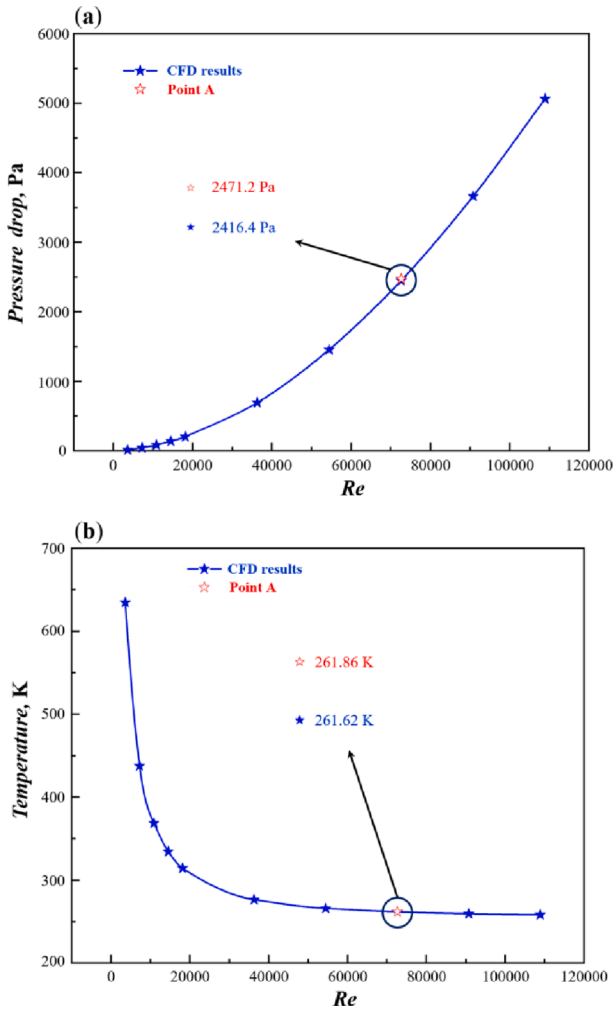


**Fig. 31.** CFD results of optimized tube and comparison with ANN prediction of Point A: (a) $\Delta P$ and (b) $T_{in}$.

that of the smooth tube. It is visible that double–symmetrical longitudinal swirls are generated in enhanced bend tube under a single upper and lower arrangement (Model D), which has the best cooling performance on the inner wall. At the studied range of *Re* (3600–127000), the *PEC* and *EEC* reach 0.99–1.18 and 0.66–1.00, respectively. In addition, it can be found that *EEC* accurately reflects thermal–hydraulic performance in the turbulence stage, while *PEC* has no apparent regularity in a range of the lower *Re*. *EEC* is more representative of thermal–hydraulic performance at the turbulent stage in the bend tube.

(3) The different parameters ($H/d$, $L/d$, $n$ and $\alpha$) of Model D are studied, of which the range is 0.5–2.5, 1.0–4.0,6–15 and 0°–90°, separately. At $Re = 72000$, the inner temperature decreases up to 4.4 K. The *Nu* and *f* increase about 9.9 %–28.8 %, 16.5 %–111.5 %, respectively, and the *EEC* reaches 0.43–0.96. It is found that under the influence of secondary circulation in the bend tube, the combination of parameters will significantly affect the distribution of longitudinal swirls. Moreover, many pairs of small vortices near the wall can improve active thermal protection performance.

(4) Orthogonal experimental design and analysis of range (ANOR) are used to simplify the sample size. The parameter $H/d$ has little effect on heat transfer enhancement when significant pressure loss occurs. Therefore, $H/d$ is fixed at 0.5 combined with the optimal results of the parameter analysis. The Pareto front shows that the design variable for the $L/d = 3.19$, $n = 11$, and $\alpha = 14.3°$ is the optimal solution by the TOPSIS selection. At $Re = 72000$, the corresponding $T_{in}$ and $\Delta P$ are 261.86 K and 2471.2 Pa. The *EEC* and *PEC* reach 1.02 and 1.09, respectively. Meanwhile, a design variable for the $L/d = 3.0$, $n = 11$, and $\alpha = 15°$ are given for ease of engineering.

Recently, there have been many types of research on heat transfer enhancement of the circular, straight tube but few studies on flow and heat transfer characteristics of the irregular–shaped bend tube. This paper designs and presents a study on discrete inclined ribs enhanced bend tube based on the DACTPS. The feasibility of realizing heat transfer enhancement by combining the secondary circulation with longitudinal swirls formed by rib turbulence is verified. At a high Reynolds number range, this method has superior thermal hydraulic performance, which meets hypersonic aircraft's active thermal protection requirements with lower pressure drop. Our paper aims to propose a new design scheme for ACTPS and provide some experience and guidance for the design of ACTPS for hypersonic aircraft.

## Declaration of Competing Interest

The authors declare that they have no known competing financial interests or personal relationships that could have appeared to influence the work reported in this paper.

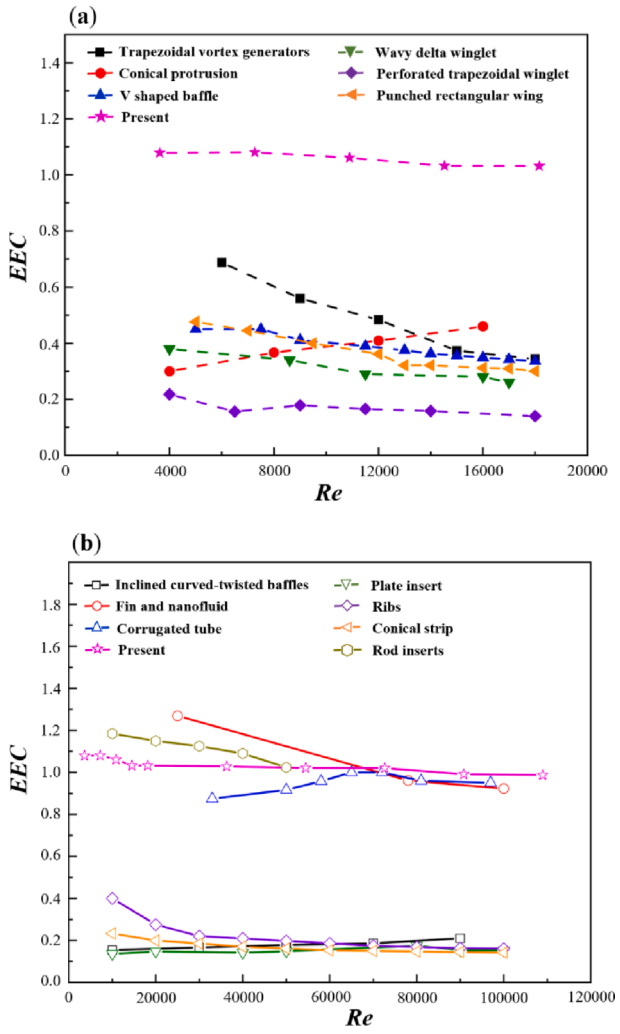


**Fig. 32.** Comparisons between present study and references: (a) Lower *Re* and (b) Higher *Re*.

## Data availability

No data was used for the research described in the article.

## Acknowledgements

This work is supported by the National Natural Science Foundation of China (Grant No. 52076008) and the Core Technology Research Project of Shunde District, Foshan City, China (No. 2130218002932).

## References

[1] M. Cui, Y. Zhao, B. Xu, et al., Inverse analysis for simultaneously estimating multi-parameters of temperature-dependent thermal conductivities of an Inconel in a reusable metallic thermal protection system[J], Appl. Therm. Eng. 125 (2017) 480–488.
[2] D. Zhang, X. Yuan, S. Liu, et al., Experimental study of wall temperature effect on shock wave/turbulent boundary layer interaction in hypersonic aircraft[J], Energy 263 (2023), 125753.
[3] Y. Sato, Y. Morino, T. Kobayashi, Research and development of thermal protection system of HOPE re-entry vehicle[J], Space Technol. Sci. (1992) 431–436.
[4] R. Ding, J. Wang, F. He, et al., Numerical investigation on the performances of porous matrix with transpiration and film cooling[J], Appl. Therm. Eng. 146 (2019) 422–431.
[5] K. El Omari, T. Kousksou, Y. Le Guer, Impact of shape of container on natural convection and melting inside enclosures used for passive cooling of electronic devices[J], Appl. Therm. Eng. 31 (14–15) (2011) 3022–3035.
[6] I. Lu, TABI-The lightweight durable thermal protection system for future reusable launch vehicles, 37th Structure, Structural Dynamics and Materials Conference, 1996, 1426.
[7] S. McCleskey, T. Strasser, P. French, et al., Development of CMC wrapped tiles for the X-38 body flap closeout panel, Space 2000 Conference and Exposition, 2000, 5311.
[8] D. Liu, X. Zheng, F. Wang, et al., Mechanism of thermomechanical coupling of high temperature heat pipe cooled C/C composite material thermal protection structure [J], Acta Materiae Compositae Sinica 27 (3) (2010) 43–49.
[9] M.M. Weislogel, M.A. Bacich, A high performance semi-passive cooling system: The Pulse Thermal Loop, Heat Transfer Summer Conference, 2004, 4692, 145–154.
[10] X. Wang, J. Ma, W. Peng, et al., Optimal design for active cooling system of hypersonic vehicle[J], Acta Aeronautica Et Astronautica Sinica 35 (3) (2014) 624–633.
[11] S. Liu, B. Zhang, Effects of active cooling on the metal thermal protection systems [J], Aerosp. Sci. Technol. 15 (7) (2011) 526–533.
[12] Y.P. Hou, C. Hou, X.P. Wan, et al., Analysis of influence parameters to convection active cooling structure[J], Guti Huojian Jishu/J. Solid Rocket Technol. 39 (1) (2016) 90–94.
[13] X. Chen, Y. Wang, Y. Long, et al., Effect of particle deposition on film cooling from fan-shaped holes[J], Int. J. Heat Mass Transf. 181 (2021), 122028.
[14] D. Mikielewicz, A. Stasiek, M. Jewartowski, et al., Measurements of heat transfer enhanced by the use of transverse vortex generators[J], Appl. Therm. Eng. 49 (2012) 61–72.
[15] S. Luo, D. Xu, J. Song, et al., A review of regenerative cooling technologies for scramjets[J], Appl. Therm. Eng. 190 (2021), 116754.
[16] Y. Zhu, W. Peng, R. Xu, et al., Review on active thermal protection and its heat transfer for airbreathing hypersonic vehicles[J], Chin. J. Aeronaut. 31 (10) (2018) 1929–1953.
[17] J. Zuo, S. Zhang, J. Qin, et al., Effects of cracking reaction on supersonic film cooling using gaseous hydrocarbon fuel as coolant[J], Appl. Therm. Eng. 171 (2020), 115134.
[18] J. Huang, W. Sun, Z. Zhang, et al., Thermal protection of electronic devices based on thermochemical energy storage[J], Appl. Therm. Eng. 186 (2021), 116507.
[19] S. Zhang, X. Li, J. Zuo, et al., Research progress on active thermal protection for hypersonic vehicles[J], Prog. Aerosp. Sci. 119 (2020), 100646.
[20] Y. Wang, P. Liu, F. Shan, et al., Effect of longitudinal vortex generator on the heat transfer enhancement of a circular tube[J], Appl. Therm. Eng. 148 (2019) 1018–1028.
[21] J. Guo, M. Xu, L. Cheng, The application of field synergy number in shell-and-tube heat exchanger optimization design[J], Appl. Energy 86 (10) (2009) 2079–2087.
[22] Z.Y. Guo, W.Q. Tao, R.K. Shah, The field synergy (coordination) principle and its applications in enhancing single phase convective heat transfer[J], Int. J. Heat Mass Transf. 48 (9) (2005) 1797–1807.
[23] J.A. Meng, X.G. Liang, Z.X. Li, Field synergy optimization and enhanced heat transfer by multi-longitudinal vortexes flow in tube[J], Int. J. Heat Mass Transf. 48 (16) (2005) 3331–3337.
[24] W. Liu, Z.C. Liu, Z.Y. Guo, Physical quantity synergy in laminar flow field of convective heat transfer and analysis of heat transfer enhancement[J], Chin. Sci. Bull. 54 (19) (2009) 3579–3586.
[25] W.Q. Tao, Z.Y. Guo, B.X. Wang, Field synergy principle for enhancing convective heat transfer—its extension and numerical verifications[J], Int. J. Heat Mass Transf. 45 (18) (2002) 3849–3856.
[26] A. Fan, J. Deng, J. Guo, et al., A numerical study on thermo-hydraulic characteristics of turbulent flow in a circular tube fitted with conical strip inserts [J], Appl. Therm. Eng. 31 (14–15) (2011) 2819–2828.
[27] H. Jia, Z.C. Liu, W. Liu, et al., Convective heat transfer optimization based on minimum entransy dissipation in the circular tube[J], Int. J. Heat Mass Transf. 73 (2014) 124–129.
[28] H. Jia, W. Liu, Z. Liu, Enhancing convective heat transfer based on minimum power consumption principle[J], Chem. Eng. Sci. 69 (1) (2012) 225–230.
[29] J. Wang, W. Liu, Z. Liu, The application of exergy destruction minimization in convective heat transfer optimization[J], Appl. Therm. Eng. 88 (2015) 384–390.
[30] J. Wang, Z. Liu, F. Yuan, et al., Convective heat transfer optimization in a circular tube based on local exergy destruction minimization[J], Int. J. Heat Mass Transf. 90 (2015) 49–57.
[31] P. Sriromreun, C. Thianpong, P. Promvonge, Experimental and numerical study on heat transfer enhancement in a channel with Z-shaped baffles[J], Int. Commun. Heat Mass Transfer 39 (7) (2012) 945–952.
[32] Y. Wang, P. Liu, H. Xiao, et al., Design and optimization on symmetrical wing longitudinal swirl generators in circular tube for laminar flow[J], Int. J. Heat Mass Transf. 193 (2022), 122961.
[33] N. Zheng, P. Liu, F. Shan, et al., Heat transfer enhancement in a novel internally grooved tube by generating longitudinal swirl flows with multi-vortexes[J], Appl. Therm. Eng. 95 (2016) 421–432.
[34] N. Zheng, W. Liu, Z. Liu, et al., A numerical study on heat transfer enhancement and the flow structure in a heat exchanger tube with discrete double inclined ribs [J], Appl. Therm. Eng. 90 (2015) 232–241.
[35] J. Cheng, Z. Qian, Q. Wang, et al., Numerical study of heat transfer and flow characteristic of twisted tube with different cross section shapes[J], Heat Mass Transf. 55 (2019) 823–844.
[36] T.A.N.G. Xinyi, Z.H.U. Dongsheng, Experimental and numerical study on heat transfer enhancement of a rectangular channel with discontinuous crossed ribs and grooves[J], Chin. J. Chem. Eng. 20 (2) (2012) 220–230.

[37] P. Gunnasegaran, H.A. Mohammed, N.H. Shuaib, et al., The effect of geometrical parameters on heat transfer characteristics of microchannels heat sink with different shapes[J], Int. Commun. Heat Mass Transfer 37 (8) (2010) 1078–1086.
[38] L. Li, X. Du, Y. Zhang, et al., Numerical simulation on flow and heat transfer of fin-and-tube heat exchanger with longitudinal vortex generators[J], Int. J. Therm. Sci. 92 (2015) 85–96.
[39] Y. Qiao, P. Liu, W. Liu, et al., Analysis and optimization of flow and heat transfer performance of active thermal protection channel for hypersonic aircraft[J], Case Stud. Therm. Eng. 39 (2022), 102476.
[40] P. Liu, N. Zheng, Z. Liu, et al., Thermal-hydraulic performance and entropy generation analysis of a parabolic trough receiver with conical strip inserts[J], Energ. Conver. Manage. 179 (2019) 30–45.
[41] B. Ji, X. Luo, Y. Wu, et al., Partially-Averaged Navier-Stokes method with modified k–ε model for cavitating flow around a marine propeller in a non-uniform wake[J], Int. J. Heat Mass Transf. 55 (23–24) (2012) 6582–6588.
[42] F.R. Menter, M. Kuntz, R. Langtry, Ten years of industrial experience with the SST turbulence model[J], Turbulence, Heat Mass Transfer 4 (1) (2003) 625–632.
[43] D.C. Wilcox, Turbulence modeling for CFD. La Canada, CA: DCW Industries, Inc, November, 2006, 34.
[44] V. Shankar, K.B.S. Rao, S.L. Mannan, Microstructure and mechanical properties of Inconel 625 superalloy[J], J. Nucl. Mater. 288 (2–3) (2001) 222–232.
[45] J.J. Liu, Z.C. Liu, W. Liu, 3D numerical study on shell side heat transfer and flow characteristics of rod-baffle heat exchangers with spirally corrugated tubes[J], Int. J. Therm. Sci. 89 (2015) 34–42.
[46] J. Yang, L. Ma, J. Bock, et al., A comparison of four numerical modeling approaches for enhanced shell-and-tube heat exchangers with experimental validation[J], Appl. Therm. Eng. 65 (1–2) (2014) 369–383.
[47] M.U. Kumar, M.M. Hussian, M.Y. Ali, Thermo Hydraulics Performance of Turbulent Flow Heat Transfer Through Square Ducts With Inserts[J], Int. J. Mech. Eng. Technol. 5 (11) (2014) 59–65.
[48] H. Xiao, Z. Dong, Z. Liu, et al., Heat transfer performance and flow characteristics of solar air heaters with inclined trapezoidal vortex generators[J], Appl. Therm. Eng. 179 (2020), 115484.
[49] V. Gnielinski, New equations for heat and mass transfer in turbulent pipe and channel flow[J], Int. Chem. Eng. 16 (2) (1976) 359–368.
[50] V. Gnielinski, On heat transfer in tubes[J], Int. J. Heat Mass Transf. 63 (2013) 134–140.
[51] T. Ochrymiuk, Numerical prediction of film cooling effectiveness over flat plate using variable turbulent Prandtl number closures[J], J. Therm. Sci. 25 (3) (2016) 280–286.
[52] X. Wang, N. Zheng, Z. Liu, et al., Numerical analysis and optimization study on shell-side performances of a shell and tube heat exchanger with staggered baffles [J], Int. J. Heat Mass Transf. 124 (2018) 247–259.
[53] J.Q. Yang, Y.R. Wang, Structural optimization of hollow fan blade based on orthogonal experimental design[J], J. Aerospace Power 26 (2) (2011) 376–384.
[54] J.L. Bently, D.F. Stanat, Analysis of range searches in quad trees[J], Inf. Process. Lett. 3 (6) (1975) 170–173.
[55] Y.C. Lee, Analysis of range and position comparison methods as a means to provide GPS integrity in the user receiver, in: Proceedings of the 42nd Annual Meeting of the Institute of Navigation, 1986, 1986: 1-4.
[56] F. Selimefendigil, H.F. Öztop, Thermal management for conjugate heat transfer of curved solid conductive panel coupled with different cooling systems using non-Newtonian power law nanofluid applicable to photovoltaic panel systems[J], Int. J. Therm. Sci. 173 (2022), 107390.
[57] A.M. Abubaker, A.D. Ahmad, A.A. Salaimeh, et al., A novel solar combined cycle integration: An exergy-based optimization using artificial neural network[J], Renew. Energy 181 (2022) 914–932.
[58] H. Lee, M. Kang, K.W. Jung, et al., An artificial neural network model for predicting frictional pressure drop in micro-pin fin heat sink[J], Appl. Therm. Eng. 194 (2021), 117012.
[59] K. Deb, A. Pratap, S. Agarwal, et al., A fast and elitist multiobjective genetic algorithm: NSGA-II[J], IEEE Trans. Evol. Comput. 6 (2) (2002) 182–197.
[60] K.P. Yoon, C.L. Hwang, Multiple attribute decision making: an introduction[M], Sage publications, 1995.
[61] J.S. Sawhney, R. Maithani, S. Chamoli, Experimental investigation of heat transfer and friction factor characteristics of solar air heater using wavy delta winglets[J], Appl. Therm. Eng. 117 (2017) 740–751.
[62] T. Alam, M.H. Kim, Heat transfer enhancement in solar air heater duct with conical protrusion roughness ribs[J], Appl. Therm. Eng. 126 (2017) 458–469.
[63] S. Skullong, P. Promthaisong, P. Promvonge, et al., Thermal performance in solar air heater with perforated-winglet-type vortex generator[J], Sol. Energy 170 (2018) 1101–1117.
[64] P. Promvonge, S. Skullong, Heat transfer augmentation in solar receiver heat exchanger with hole-punched wings[J], Appl. Therm. Eng. 155 (2019) 59–69.
[65] P. Promvonge, Heat transfer and pressure drop in a channel with multiple 60 V-baffles[J], Int. Commun. Heat Mass Transfer 37 (7) (2010) 835–840.
[66] H. Xiao, P. Liu, Z. Liu, et al., Performance analyses in parabolic trough collectors by inserting novel inclined curved-twisted baffles[J], Renew. Energy 165 (2021) 14–27.
[67] A. Mwesigye, T. Bello-Ochende, J.P. Meyer, Heat transfer and thermodynamic performance of a parabolic trough receiver with centrally placed perforated plate inserts[J], Appl. Energy 136 (2014) 989–1003.
[68] B. Amina, A. Miloud, L. Samir, et al., Heat transfer enhancement in a parabolic trough solar receiver using longitudinal fins and nanofluids[J], J. Therm. Sci. 25 (2016) 410–417.
[69] W. Fuqiang, T. Zhexiang, G. Xiangtao, et al., Heat transfer performance enhancement and thermal strain restrain of tube receiver for parabolic trough solar collector by using asymmetric outward convex corrugated tube[J], Energy 114 (2016) 275–292.
[70] C. Chang, A. Sciacovelli, Z. Wu, et al., Enhanced heat transfer in a parabolic trough solar receiver by inserting rods and using molten salt as heat transfer fluid[J], Appl. Energy 220 (2018) 337–350.
[71] P. Liu, J. Lv, F. Shan, et al., Effects of rib arrangements on the performance of a parabolic trough receiver with ribbed absorber tube[J], Appl. Therm. Eng. 156 (2019) 1–13.